



Regional CO₂ and CH₄ inversion system using WRF-Chem (v4.4)/DART (v9.8.0) and continuous high-precision observations over the Korean Peninsula

Doyoon Kwon¹, Bonhoon Koo¹, Jooyeop Lee¹, Jeongwon Kim¹, Jaehyung Ahn¹, Jinkyu Hong¹, Eri Saikawa², Alexander Avramov², Changsub Shim³, Je-Woo Hong³, Daegeun Shin⁴, Shanlan Li⁴, Sumin Kim⁴, and Sangwon Joo⁴

Correspondence to: Jinkyu Hong (jhong@yonsei.ac.kr)

Abstract. We develop a high-resolution dual-species greenhouse gas (GHG) top-down inversion framework by integrating the Weather Research and Forecasting model coupled with Chemistry (WRF-Chem v4.4) and the Data Assimilation Research Testbed (DART v9.8.0). This framework jointly performs the assimilation of near-surface CO₂ and CH₄ concentrations alongside standard meteorological data across the Korean Peninsula. To improve the simulation of GHG turbulent dispersion in the atmospheric boundary layer over complex terrain, we incorporate surface heterogeneity parameterizations (roughness sublayer and canopy height) into the model physics in the inversion system. The system assimilates continuous in situ observations from three World Meteorological Organization/Global Atmosphere Watch (WMO/GAW) stations and produces dynamically consistent updates of CO2 and CH4 emissions. Prior flux estimates include anthropogenic emissions (EDGAR v8.0), biogenic exchanges (the region-optimized VPRM), biomass burning (FINN v2.5 data), and oceanic CO₂ exchanges (SeaFlux data). In a 2020 case study, the top-down estimates improve the agreement with ground observations, reducing rootmean-square errors by 30-60 % and correcting bias error of 1-10 ppm and 30-60 ppb for surface CO₂ and CH₄ concentrations at the high-precision surface observatory respectively. Independent aircraft profiles suggest consistency between the boundary and prior CH₄ emissions. The posterior anthropogenic emissions show decreases over the Seoul Metropolitan Area and western coastal sources for CO₂ and increases over agricultural areas for CH₄, indicating potential areas that need to refine the global emission inventories. The posterior annual national total emissions for CO₂ and CH₄ fall within the ranges reported in the Republic of Korea's Biennial Transparency Report of Korea). This case study demonstrates the utility of an observationconstrained top-down framework in supporting the Measurement-Monitoring-Reporting-Verification (MMRV) framework for national and sub-national assessments of GHG emissions and provide a scalable path toward multi-platform (satellite, aircraft, shipborne) integration.

¹Department of Atmospheric Sciences, Yonsei University, Seoul, 03722, Republic of Korea

²Department of Environmental Sciences, Emory University, Atlanta, GA, 30319, USA

³Korea Environment Institute, Sejong, 30147, Republic of Korea

⁴National Institute of Meteorological Sciences, Jeju-do, 63568, Republic of Korea





1 Introduction

Anthropogenic emissions of greenhouse gases (GHGs) originate predominantly from fossil fuel combustion, land-use change, agricultural practices, and waste management. These emissions are the principal drivers of contemporary climate change. Reliable and continuous monitoring of anthropogenic GHG emissions is essential for the development of effective climate mitigation strategies, compliance with international climate agreements, and the formulation of informed policy decisions (IPCC, 2021; Friedlingstein et al., 2025). Under the Paris Agreement, national inventories serve as the principal reporting mechanism, delineating Nationally Determined Contributions (NDCs) and facilitating periodic stocktakes (UNFCCC, 2015). These inventories are a standard method within the Measurement-Monitoring-Reporting-Verification (MMRV) framework and rely on bottom-up methodologies based on activity data and emission factors within a tiered framework established by the Intergovernmental Panel on Climate Change (IPCC) (Ogle et al., 2013). However, their accuracy is often limited by incomplete or outdated activity data, coarse spatio-temporal resolution, diffusive GHG emissions, and systemic delays in updating or reporting inventories (Rogelj et al., 2016; Pauw et al., 2018). Even nations with advanced inventories encounter challenges in capturing rapid emission changes, fine-scale spatial heterogeneity, and localized sources, which undermines the inventory credibility and comparability of inventories (Denison et al., 2019; Nisbet et al., 2019; WMO, 2025).

Top-down approaches, which are based on atmospheric inverse modeling or atmospheric data assimilation (DA), offer independent assessments of emissions by constraining surface fluxes through atmospheric concentration measurements (Enting, 2002; Gurney et al., 2002; Weiss and Prinn, 2011; Oda et al., 2019; Janssens-Maenhout et al., 2020; Elguindi et al., 2020; Mueller et al., 2021; Deng et al., 2022; WMO, 2025). These methodologies are increasingly incorporated into MMRV frameworks (WMO, 2022; 2025). By reconciling observed atmospheric concentrations with emission fluxes, top-down approaches can identify unreported or misrepresented emission sources, detect biases, and provide spatially explicit, policy-relevant emission information (Mueller et al., 2021; Janssens-Maenhout et al., 2020). Recent advancements in observational infrastructure, including dense atmospheric observation networks, satellite platforms, and airborne measurements, have enabled top-down systems to resolve emission patterns at urban and sub-national scales, thereby enhancing the fidelity and applicability of MMRV systems (Lauvaux et al., 2020; Byrne et al., 2023; Velasco et al., 2023).

Atmospheric inverse modeling frameworks for GHGs typically employ either Lagrangian or Eulerian methodologies. Lagrangian-based inversion frameworks track air parcels backward from receptor sites, offering computationally efficient source attribution (e.g., Henne et al., 2016; Pisso et al., 2019; Sijikumar et al., 2023; Brunner et al., 2025; Bukosa et al., 2025). However, they depend on external meteorological fields and background GHG concentrations, which limits their capability to accurately represent complex boundary-layer dynamics (Bréon et al., 2015; Lauvaux et al., 2016; Dekker et al., 2017; Super et al., 2017; Gaudet et al., 2021; Nalini et al., 2022; Bukosa et al., 2025). Conversely, Eulerian frameworks solve advection-diffusion equations directly on fixed spatial grids, allowing for a physically consistent coupling of meteorology and tracer transport, particularly when integrated with ensemble-based DA techniques such as the Ensemble Adjustment Kalman Filter (EAKF) (Anderson, 2001; Kang et al., 2012; Gaudet et al., 2021). Notable examples of operational Eulerian systems include



80



the NOAA (National Oceanic and Atmospheric Administration) CarbonTracker (van der Velde et al., 2018) and ECMWF (European Centre for Medium-Range Weather Forecasts)'s CAMS (Copernicus Atmosphere Monitoring Service) global reanalysis (Agustí-Panareda et al., 2023); however, these systems typically operate at relatively coarse resolutions of about 1° which limits their effectiveness in capturing fine-scale emission heterogeneity in urban or mountainous regions (Gurney et al., 2002; Locatelli et al., 2013; Zhang et al., 2014; Feng et al., 2019; Gaudet et al., 2021).

These limitations necessitate the development of high-resolution Eulerian DA frameworks capable of the simultaneous assimilation of multiple greenhouse gas species, especially in complex terrains and regions characterized by heterogeneous land use and land cover. The Weather Research and Forecasting model coupled with Chemistry (WRF-Chem) provides high-resolution, online coupling of meteorology and chemistry, while the Data Assimilation Research Testbed (DART) offers a robust ensemble-based DA platform for dynamically updating meteorological and chemical states resolution. Accordingly, the WRF-Chem coupled with the DART has been used in CO₂ concentration, regional meteorology and air quality studies (e.g., Mizzi et al., 2018; Ma et al., 2020; Zhang et al., 2021a). Despite its successful applications in regional meteorology and air quality, the application of WRF-Chem and DART to dual-species (CO₂ and CH₄) greenhouse gas inversions remains limited, particularly at the fine spatial scales necessary for policy support and effective integration into national MMRV systems over complex landscapes.

This study advances the WRF-Chem (v.4.4) and DART (v.9.8.0) modeling framework by implementing a high-resolution (9 km) dual-species inversion system for the simultaneous assimilation of meteorology and CO₂ and CH₄ concentrations. Notably, we integrate model physics parameterizations and land information into the inversion system, explicitly tailored to the complex terrain and clustered emission patterns of the Korean Peninsula. The distinctive geographical and climatological attributes of Korea, including complex topography, densely populated urban environments, concentrated industrial sources, and pronounced seasonal monsoon variability pose significant challenges for the quantification and verification of emissions using conventional inventories, micrometeorological measurements and lower-resolution inversion methodologies (e.g., Hong and Kim, 2011; Hong et al., 2019; Hong et al., 2020; Lee et al., 2021; Kim et al., 2024). We describe the developed dual inversion framework, then evaluate the 2020 application through quantitative assessments of concentration/flux error reductions and intercomparisons with multiple emissions datasets, demonstrating the framework's utility for sub-national monitoring and MMRV.

2 Description of CO2 and CH4 inversion framework

2.1 Atmospheric modeling system

Our GHG inversion framework integrates a regional Eulerian atmospheric chemistry model with an ensemble-based data assimilation system. Specifically, this framework employs the Weather Research and Forecasting model coupled with Chemistry (WRF-Chem v4.4; Grell et al., 2005) and the Data Assimilation Research Testbed (DART v9.8.0) (Anderson et al., 2009) for sequential data assimilation. WRF-Chem solves the fully compressible, nonhydrostatic Eulerian equations on a fixed



105

110

115



spatial grid, and simulates atmospheric dynamics, physical and chemical processes, and chemical transport within a unified framework.

In the inversion system, WRF-Chem generates ensemble forecasts by simulating meteorology with surface fluxes and atmospheric transport processes of GHGs. Given the long atmospheric lifetime of GHGs, they have been simulated as passive tracers in mesoscale models (Dekker et al., 2017; Super et al., 2017; Zhao et al., 2023). WRF-Chem includes the module to simulate passive tracer transport of GHGs since WRF-Chem v3.4 (Beck et al., 2012). In WRF-Chem, distinct variables represent background, anthropogenic, biomass-burning, oceanic (CO₂ only), and biogenic components of CO₂ and CH₄. The model simulates their fluxes, transport, and diffusion processes driven by the meteorological field to obtain a three-dimensional concentration field on an hourly basis. The total concentrations are represented as the sum of the component variables, facilitating comparison with observed concentrations.

Notably, for better simulations of GHG transport over complex terrain, we used the revised WRF-Chem by replacing the default WRF canopy height with high-resolution (1km) spaceborne lidar-retrieved canopy height data (GLAS/ICESat) for a better representation of surface characteristics (Lee and Hong, 2016). To simulate realistic transport and dispersion of GHG in the PBL, we further adapted roughness sublayer (RSL) parameterization of Lee et al. (2020), which incorporated the RSL function from the unified theory of Harman and Finnigan (2007, 2008) and Harman (2012), into the revised MM5 surface layer scheme (Jiménez et al., 2012) and Noah land surface model in WRF. Hereafter, we refer to this modified WRF-Chem v4.4 as the WRF-Chem GHG.

Our study area consists of a single model domain with 9-km horizontal spacing of 97 ×136 grid points and 51 terrainfollowing vertical levels stretching from the surface up to 50 hPa at the upper boundary (Fig. 1). The model employed specific physics parameterization schemes (Kim et al., 2024 and references therein), including the WSM-6 microphysics, RRTMG shortwave and longwave radiation schemes, the Yonsei University scale-aware PBL scheme, Kain-Fritsch cumulus scheme, and the Unified Noah Land Surface Model (LSM).

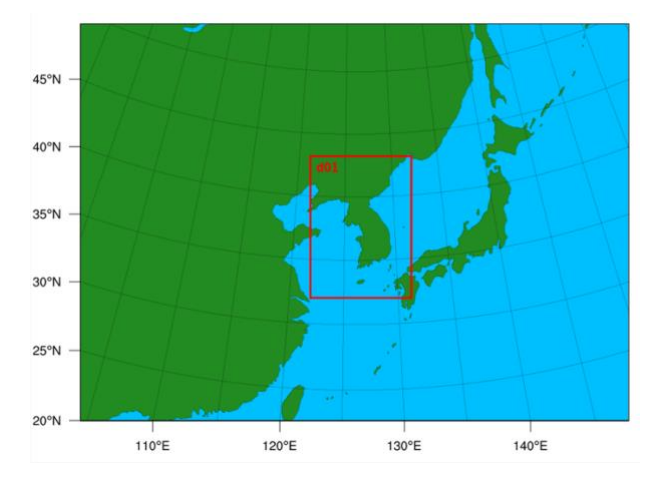


Figure 1. The WRF-Chem domain configuration used in this study.



125

130

135

140

145

150



2.2 DART data assimilation for GHG inversion

DART serves as a modular DA system designed to interface with various atmospheric models and observational datasets. The integration of WRF-Chem and DART enables the simultaneous assimilation of meteorological variables and chemical species, making physically consistent updates across the coupled system (Mizzi et al., 2016; Mizzi et al., 2018). The system operates as an ensemble of WRF-Chem forecasts, with each member representing a perturbed version of the state vector that accounts for observational and model uncertainties. At each analysis cycle, ensemble perturbations are utilized to estimate flow-dependent background error covariance, enabling the Ensemble Adjustment Kalman Filter (EAKF) to adjust both meteorological and tracer fields simultaneously in a dynamically balanced manner. This ensemble-based structure allows for uncertainty propagation, progressive enhancement of prior estimates, and the maintenance of consistency between state variables during sequential assimilation. Hereafter, we refer to the WRF-Chem GHG coupled with DART (v.9.8.0) as the WRF-Chem/DART.

Our work extends the DA system to facilitate the simultaneous assimilation of observed CO₂ and CH₄ concentrations with meteorological data at a spatial resolution of 9 km over the Korean Peninsula. Notably, meteorological and GHG tracer fields evolve within the coupled modeling framework, eliminating the need for externally prescribed meteorological fields or offline drivers. This approach generates dynamically consistent reanalysis fields and emission estimates tailored to the regional transport environment. The assimilated data include continuous *in situ* CO₂ and CH₄ concentrations, alongside standard meteorological observations from National Centers for Environmental Prediction automated data processing upper air and surface observations (PREPBUFR observations). All variables are jointly updated within the ensemble state vector, thereby allowing for the dynamic co-evolution of GHG concentrations and meteorological fields. This update process facilitates feedback between meteorology and tracer transport and improve the physical consistency and estimation skill of ensemble members, thereby enhancing the quality of transport and flux estimation in the WRF-Chem/DART framework accordingly.

Analyses are produced every six hours (at 00, 06, 12, 18 UTC), using observations within a ± 3 h window centered on the analysis time. Observation values are rejected if they exceed three standard deviations of the background ensemble. The analysis ensemble is then advanced with WRF-Chem for a six-hour forecast, which provides the background for the next cycle. Prior uncertainty is represented by Gaussian perturbations of ± 5 % (1 σ) to chemical initial and lateral boundary conditions and ± 30 % to anthropogenic fluxes. Covariance localization uses a Gaspari–Cohn polynomial with a horizontal half-width of 0.025 rad (~ 150 km) and a vertical half-width of 10 km, constraining increments primarily to the lower troposphere and reducing under-sampling error (Gaspari and Cohn, 1999; Anderson, 2012; Kang et al., 2012). Cross-species covariances are not applied; CO₂ and CH₄ tracers are updated independently.



160

165



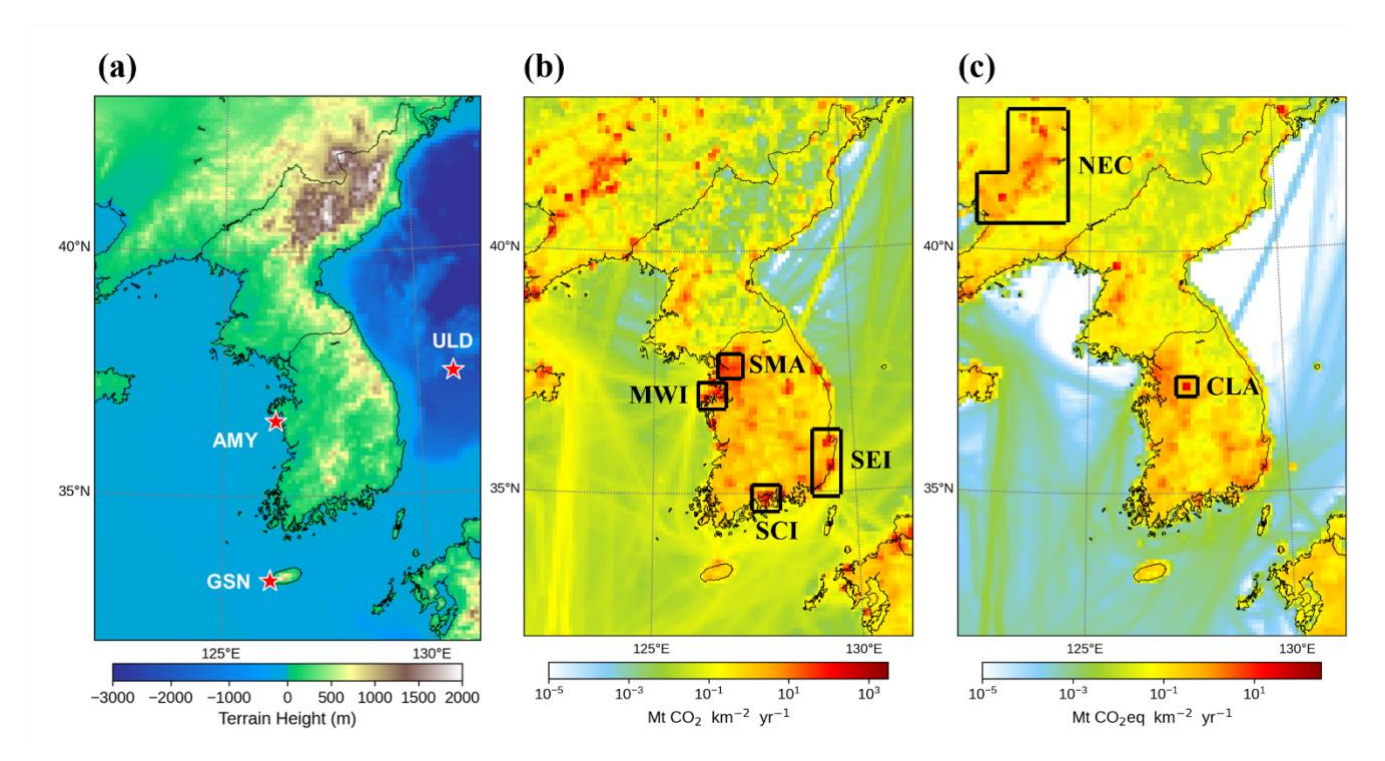


Figure 2. Locations of GHG monitoring stations (AMY, GSN, ULD) over terrain height (a) and annual anthropogenic emissions of CO₂ (b) and CH₄ (c) in the model domain in 2020 from EDGAR (v8.0). Main emission source regions in the model domain are boxed: (SMA: the Seoul Metropolitan Area, MWI: Mid-Western Industrial Area, SEI: SouthEastern Industrial Area, SCI: South Coast Industrial Area, CLA: Central Livestock Area, NEC: NorthEastern China).

3 Observation data of GHG concentrations and meteorological conditions for data assimilation

High-precision, continuous ground-based GHG measurements are essential for resolving fine-scale spatio-temporal variability in atmospheric composition and evaluating surface fluxes near major source regions. To constrain CO₂ and CH₄ fields in our inversion system, the inversion framework assimilates *in situ* measurements of CO₂ and CH₄ concentrations from World Meteorological Organization (WMO) Global Atmosphere Watch (GAW) affiliated monitoring stations at Anmyeondo (AMY), Gosan, Jeju Island (GSN), and Ulleungdo (ULD) operated by the Korea Meteorological Administration (Fig. 2a). Depending on wind direction and atmospheric stability, they sample background inflow and downwind plumes from key emission source regions (Fig. 2b and 2c). In addition, we simultaneously assimilate standard meteorological observations from the National Centers for Environmental Prediction (NCEP) PREPBUFR datasets which includes surface pressure, air temperature, wind speed and direction, specific humidity, sea surface temperature, and satellite-derived upper-air profiles.



170

180

185

190



Each site employs a harmonized measurement system based on cavity ring-down spectroscopy (CRDS, Picarro Inc., USA), paired with a custom cryogenic drying system jointly developed by KMA and the Korea Research Institute of Standards and Science (KRISS). This setup ensures high-precision CO₂ and CH₄ measurements with minimal water vapor interference, critical for ensuring data quality under Korea's seasonally variable meteorological conditions. Data are collected at 1-minute intervals, processed hourly into Level-2 quality-assured products, and include intake heights of 40 m (AMY), 12 m (GSN), and 10 m (ULD). Further details on instrument calibration, QA/QC protocols, and traceability to international standards for CO₂ and CH₄ observations at WMO/GAW sites in Korea can be found in Lee et al. (2019) and Lee et al. (2023).

4 Initial and boundary conditions for meteorological variables and GHG concentrations

Meteorological initial and boundary conditions are obtained from ERA5 global reanalysis hourly single and pressure-level data at 0.25° × 0.25° resolution (Hersbach et al., 2020; Hersbach et al., 2023a, 2023b). The initial and boundary conditions are preprocessed by WRF Preprocessing System (WPS) at the model grids and then perturbed by WRF Data Assimilation System (WRFDA) based on previous studies (Barker et al., 2012; Mizzi et al., 2016; Liu et al., 2017; Zhang et al., 2021b).

Initial and boundary conditions of CO_2 and CH_4 are provided by the ECMWF CAMS global greenhouse-gas reanalysis (EGG4 hereafter) data (Inness et al., 2019; Agustí-Panareda et al., 2023). EGG4 applies 4D-Var data assimilation of *in situ* networks and satellite retrievals within the ECMWF's Integrated Forecast System (IFS Cycle 47R1) and currently covers the period of 2003–2020. The dataset provides atmospheric mixing ratio of CO_2 and CH_4 , along with meteorological and chemical variables on regular $0.75^{\circ} \times 0.75^{\circ}$ grid on 25 pressure levels and 60 hybrid σ -pressure vertical levels at 3-hourly intervals. EGG4 data as initial and lateral boundary conditions helps to ensure that large-scale seasonal and regional variability and the growing season CO_2 drawdown is represented in the background fields (not shown here).

Overall errors in CO₂ and CH₄ concentrations are within 10 ppm and 40 ppb near the earth surface (Agustí-Panareda et al., 2023). Validation of EGG4 data against Total Carbon Column Observing Network (TCCON) measurement shows standard deviations of the difference of 1.18 ppm for XCO₂ and 11.3 ppb for XCH₄ (Wang et al., 2023). Notably, it has been reported that EGG4 data have positive bias of CO₂ concentration in high emission regions, and its mean bias is about 7.46 ppm in Asia (Custódio et al., 2022). A negative bias of about 30 ppb in CH₄ concentration has been reported at the NOAA flask site in the mid-western industrial region (MWI) (Segato et al., 2025).

5 Prior fluxes

5.1 Anthropogenic emissions

Within the domain, WRF-Chem simulates GHG transport and adds contributions from local surface emissions and sinks. Anthropogenic CO₂ and CH₄ emissions as prior information are regridded from EDGAR global GHG emission inventory version 8.0 (Crippa et al., 2023). EDGAR provides anthropogenic emissions data in accordance with IPCC-compliant



200

205

210



methodologies based on international activity data and emission factors (Janssens-Maenhout et al., 2019, Crippa et al., 2024). Annual spatial distributions of CO_2 and CH_4 emissions across the domain are shown in Fig. 2. To consider temporal variability in CO_2 emission by human activities, we apply the monthly and diel scaling factor reported by the EDGAR and the gridded Temporal Improvements for Modelling Emissions by Scaling (TIMES) factors, respectively, which account for building heating/cooling usage patterns, traffic volume fluctuations, sectoral contributions (residential, commercial, transportation emission), and weekdays-weekend differences at $0.25^{\circ} \times 0.25^{\circ}$ resolutions (Nassar et al., 2013). For ocean grid cells EDGAR emission are near zero excluding shipping lanes.

The spatial distribution of annual anthropogenic CO₂ and CH₄ emissions highlights main source regions within the model domain (Fig. 2b and 2c). Strong CO₂ emission in the Seoul Metropolitan Area (SMA) reflects aggregated contributions from power plants, traffic and building emissions in urban area. Industrial processes and power generation dominate emissions in the MWI and south and southeastern coast industrial corridors (SCI and SEI) over the Korean Peninsula. Strong CO₂ emission in northeastern China (NEC) is related to power industry and combustion for manufacturing (Fig. S1). CH₄ sources are generally coincident with strong CO₂ emission regions due to waste management in high populated area but exhibits more spatially confined peaks with hotspots over the high-density urban area (SMA) (wastewater and landfills), central livestock area (CLA) (enteric fermentation and manure management), and northeastern region in China (NEC) (wastewater, landfills, and agricultural soil) (Fig. S2).

5.2 Biomass burning emissions

Biomass burning emissions of CO₂ and CH₄ are taken from the Fire Inventory from NCAR (FINN version 2.5). This data estimates biomass burning emissions using burned-area calculations, year-specific land cover and vegetation datasets, fuel loading and emission factors, and the use of multiple fire-detection satellites such as MODerate resolution Imaging Spectroradiometer (MODIS) and Visible Infrared Imaging Radiometer Suite (VIIRS) (Schroeder et al., 2014). The FINN dataset provides 1 km spatial and daily temporal resolution emissions (Wiedinmyer et al., 2011; Callewaert et al., 2022; Wiedinmyer et al., 2023). The site-specific emission data is extracted into the model grid for the WRF-Chem GHG simulations by the NCAR fire-emission preprocessing tool. Biomass burning emissions show strong spatial and seasonal variability across East Asia (Fig. S3 for CO₂ and Fig. S4 for CH₄). Biomass burning emission over the Korean Peninsula is negligible compared to other sources and sinks. The peaks in northeastern China during the spring (March–May) are related with agricultural residue burning and land-clearing practices.

225 5.3 Ocean CO₂ exchanges

Air-sea CO₂ exchange is obtained from the latest SeaFlux Ocean Carbon Dioxide Flux product (v2023.02) (Roobaert et al., 2018; Fay et al., 2021; Roobaert et al., 2019). This dataset combines five meteorological reanalysis data with six ocean surface



230

235

240

245

250

255



CO₂ datasets, making a total of 30 combinations of the data products. These data provide monthly ocean CO₂ fluxes on a 1°x1° grid for 1990-2022. For this study, ensemble-mean monthly exchanges are used for oceanic CO₂ fluxes. Monthly distribution of oceanic CO₂ exchanges over East Asia shows that the Yellow Sea (average depth ~50 m) and nearby shelves exhibit seasonal reversals in oceanic CO₂ fluxes (i.e., net uptake during winter and spring and a source in summer) (Fig. S5)(Gregor and Fay, 2021). In contrast, the deeper East Sea (average depth ~1500 m) acts as a persistent CO₂ sink. Although these patterns reflect known contrasts between shallow shelves and deep basins, the oceanic flux magnitude in this domain is small relative to dominant anthropogenic and terrestrial biogenic CO₂ sources and sink.

5.4 VPRM-based estimation of terrestrial ecosystem fluxes

Terrestrial ecosystem carbon fluxes are estimated with the Vegetation Photosynthesis and Respiration Model (VPRM) coupled with the WRF-Chem. (Ahmadov et al., 2007; Mahadevan et al., 2008). VPRM simulates net ecosystem exchange (NEE) of CO₂ using meteorological drivers and satellite-derived surface indices, specifically the Enhanced Vegetation Index (EVI) and Land Surface Water Index (LSWI) from MODIS Terra surface reflectance 8-Day 500m product (MOD09A1). During model integration, VPRM dynamically computes the sum of gross primary production (GPP) and respiration (RES) for eight land-cover categories using EVI, LSWI, 2 m air temperature, and downward shortwave radiation simulated by the WRF-Chem. Vegetation inputs (plant functional type, EVI, and LSWI) are derived from the 1-km SYNMAP global land cover data and MOD09A1 and are preprocessed using the VPRM preprocessor (Jung et al., 2006). VPRM-derived terrestrial CO₂ fluxes are sensitive to parameters linking EVI, LSWI, temperature, and radiation to GPP and RES (Hilton et al., 2013; Dayalu et al., 2018; Li et al., 2020). Because each vegetation type has distinct responses to environmental drivers, parameter calibration is critical to reduce NEE biases with plant function types. In this study, we adopt the parameter values from Li et al. (2020) calibrated for East Asian land-cover conditions to better capture seasonal and ecological variations across the Korean Peninsula.

Terrestrial biogenic CO₂ fluxes from the VPRM shows strong seasonality driven by photosynthetic activity and temperature-

dependent respiration (Fig. 3). Croplands, deciduous and mixed forests dominate in the model domain and contribute most to net carbon uptake during the growing summer season (Fig. 3). Savanna and shrubland play minor roles in total uptake due to their limited areal extent. Monthly NEE shows clear net carbon uptake (negative values) in summer growing season (May to September) with the strongest uptake (i.e., most negative NEE) in July when GPP exceeds RES with relatively larger uncertainties in biogenic CO₂ fluxes. The monthly mean diurnal cycles of GPP, RES, and NEE further highlights daytime GPP peaks in summer mainly driven by higher incoming shortwave radiation and by more gradual, temperature-driven RES with the seasonal march of the summer monsoon (Fig. S6) (Hong et al., 2011). For 2020, the domain-integrated NEE over South Korea is -43 Mt CO₂ (5% of national anthropogenic GHG emissions) and broadly consistent with the national inventory estimate of the LULUCF sink (-39 Mt CO₂; Ministry of Environment, Republic of Korea, 2025), indicating that the VPRM biogenic fluxes reasonably represent the terrestrial carbon sink in this system.



275

280



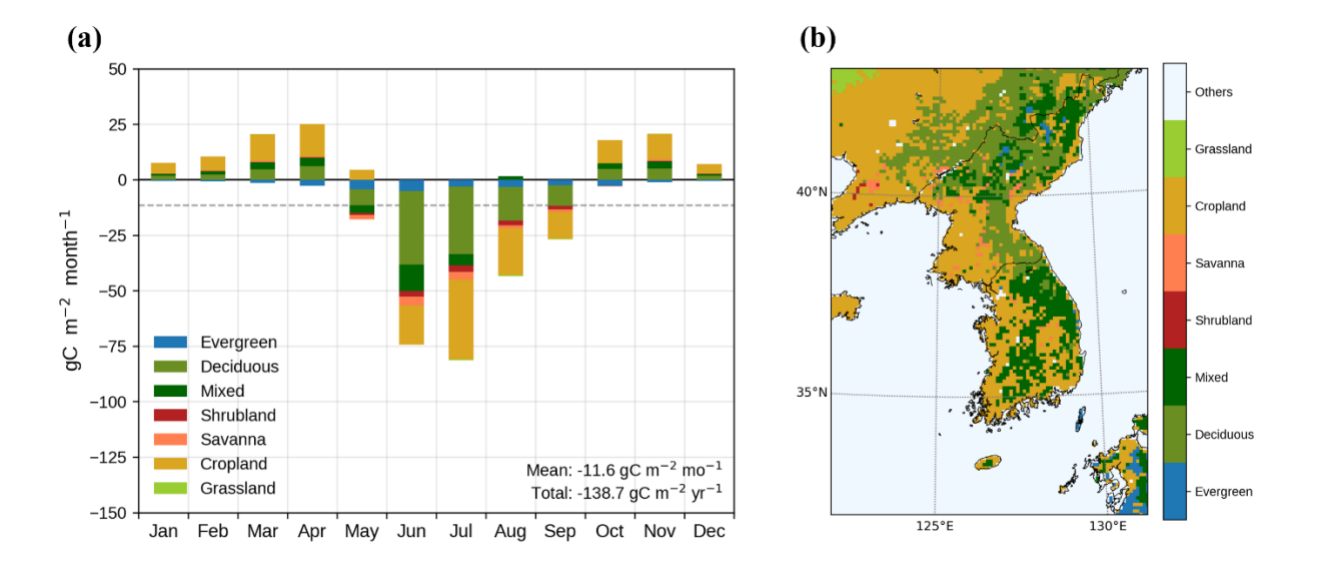


Figure 3. (a) Monthly net ecosystem exchange (NEE) contributions by vegetation class over the model domain in 2020. Bars show class totals (g C m⁻² month⁻¹), computed as spatial averages over grid cells of the corresponding vegetation type; negative values indicate net carbon uptake. (b) Spatial distribution of dominant vegetation classes used in WRF-Chem/VPRM; each grid cell is assigned the class with the largest vegetation fraction. Colors are consistent across panels.

6 Evaluation of the top-down estimates for 2020 case study

We evaluated inversion results for 2020 using the WRF-Chem/DART system with full DA, in which both meteorological and GHG observations were assimilated. Each monthly run was initiated at 00 UTC on the last day of the preceding month, followed by a 24-hour spin-up prior to the start of assimilation.

270 6.1 GHG concentrations at ground stations

Monthly distributions of prior, posterior, and observed CO₂ and CH₄ concentrations at the three WMO/GAW surface stations are summarized with box plots for comparison of seasonal variability and site-to-site statistics (Fig. 4 and Table 1). Prior CO₂ concentrations overestimate the *in situ* observations at the AMY by about 12 ppm but underestimate at the remote stations (ULD and GSN) by 2-3 ppm. Prior CH₄ concentrations underestimate at all the stations especially during summer season by 15 ppb. These biases are well matched with uncertainties in the boundary data from the EGG4. The top-down estimates of GHG concentrations show markedly improved agreement with observations relative to the prior, thus demonstrating the efficacy of the EAKF assimilation in adjusting surface GHG concentrations. At the observation locations, the posterior estimates generally fall between the prior and the observations and across all sites and both species, posterior estimates consistently reduce MBE (mean bias error), RMSE (root mean square error) (Table 1). Mean bias of posterior surface CO₂ and CH₄ concentrations are in the range of 1-2 ppm and 20-30 ppb, respectively. The largest error improvements of CO₂ and CH₄ concentrations are at AMY and GSN, and their corresponding error reductions are 10.9 ppm and 57 ppb, respectively. Error



290



reductions are most pronounced in summer, consistent with corrections to low-biased boundary inflow for CH₄ and to underrepresented seasonal regional fluxes (e.g., anthropogenic and biogenic contributions) when seasonal gradients are largest.

Notable differences are evident in the skewness of the monthly distributions of observed CO₂ and CH₄ concentrations across the sites. At AMY, both prior and posterior CO₂ and CH₄ exhibit strong positive skew and higher variability (elongated upper whiskers in Fig. 4a and 4d), depending on wind around nearby large point sources (i.e., power and industrial plants in the MWI). In contrast, GSN and ULD show more symmetric, compact distributions, suggesting weaker local source influence on these remote stations. All three stations exhibit a pronounced summertime dip in CH₄ concentration, especially in August, consistent with enhanced OH-driven atmospheric oxidation under warm, humid, and high-radiation conditions (East et al., 2024). This seasonal signal is stronger at the lower-latitude sites (AMY, GSN), where oxidation capacity becomes stronger. Similar dips appear in the EGG4 data used as lateral boundary forcing in WRF-Chem GHG (see Fig. S9), indicating that the seasonal CH₄ decline is largely imposed by large scale features.

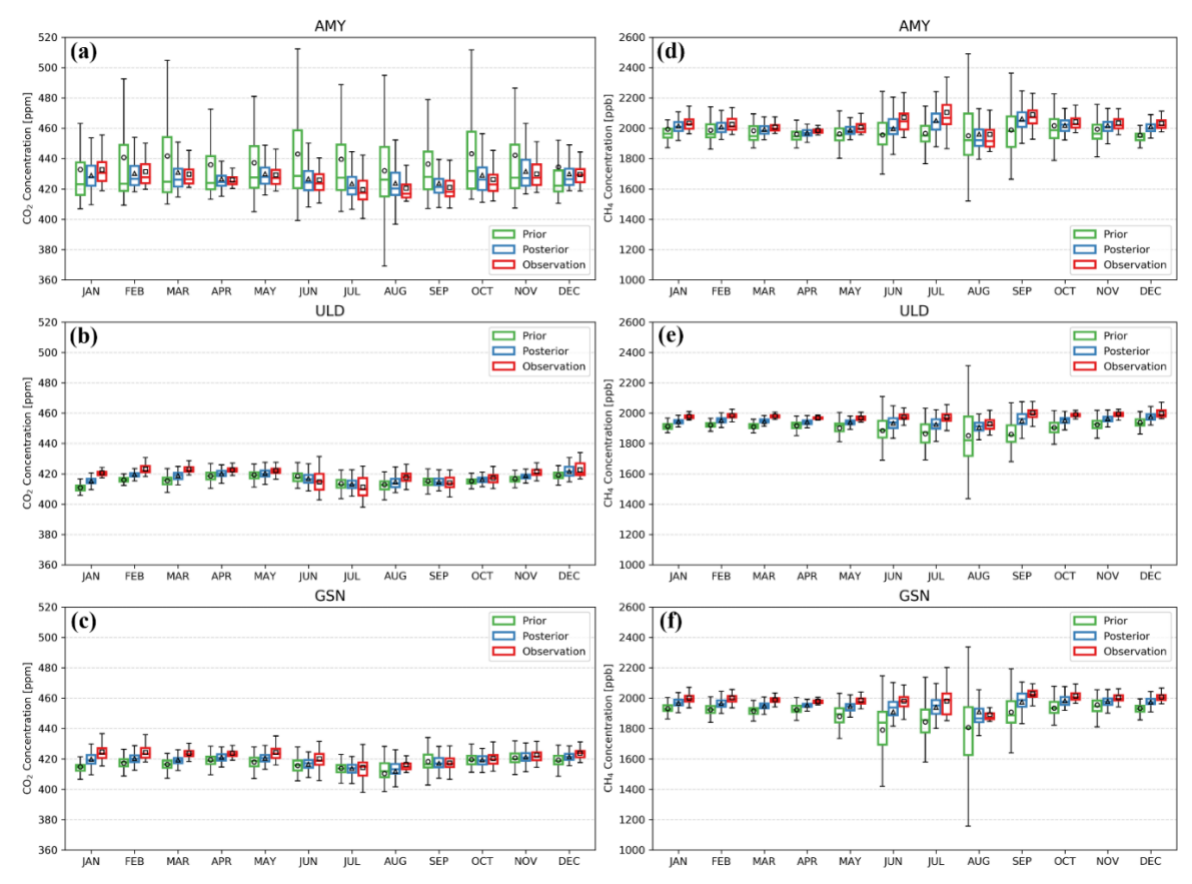


Figure 4. Monthly boxplots of CO₂ (a-c) and CH₄ (d-f) concentrations at AMY (a,d), ULD (b,e), and GSN (c,f) in 2020. Prior (green), posterior (blue), and observations (red) are shown for each site. Boxes denote the interquartile range (25th-75th percentiles); horizontal lines indicate medians. Filled symbols denote means (prior: circle; posterior: triangle; observation: square).





Table 1. Mean bias error (MBE) and root-mean-square error (RMSE of the top-down estimates to the observations at AMY, ULD, and GSN in 2020. Statistics are computed from 6-hourly averages.

Station name	Latitude	Longitude	GHG variable	MBE	RMSE
AMY	36.53°N	126.32°E	Prior CO ₂	12.1 ppm	35.2 ppm
			Posterior CO ₂	1.2 ppm	13.9 ppm
			Prior CH ₄	-52 ppb	163 ppb
			Posterior CH ₄	-23 ppb	111 ppb
ULD	37.48°N	130.90°E	Prior CO ₂	-2.4 ppm	7.7 ppm
			Posterior CO ₂	-1.2 ppm	5.4 ppm
			Prior CH ₄	-72 ppb	124 ppb
			Posterior CH ₄	-30 ppb	60 ppb
GSN	33.29°N	126.16°E	Prior CO ₂	-3.4 ppm	10.0 ppm
			Posterior CO ₂	-2.3 ppm	7.4 ppm
			Prior CH ₄	-88 ppb	179 ppb
			Posterior CH ₄	-31 ppb	109 ppb

6.2 Validation against aircraft observations

305

310

To independently evaluate the performance of the inversion system, posterior CO₂ and CH₄ concentrations are compared with aircraft-based *in situ* observations collected over the Yellow Sea near the AMY station in 2020 using a Beechcraft King Air 350. The aircraft was equipped with a CRDS (G2401, Picarro Inc., USA) for measuring CO₂, CH₄, CO, and H₂O, at a sampling rate of 1.5 Hz. Sample air was dried upstream, and inlet ports were located near the front fuselage to minimize contamination. Typical operating altitudes reached 10 km with cruising speeds of 70–120 m s⁻¹, supporting both routine profiling and regional transport characterization. Ten vertical profile flights near the AMY were available in 2020 (not used in the data assimilation) (Fig. S7). After quality control, the profiles were aggregated into 1 km altitude bins (±500 m). For each bin, we computed mean observed concentrations and observational uncertainties (quadrature of sampling variability and reported measurement uncertainty) alongside the corresponding posterior values.

Figure 5 presents vertical profiles for CO₂ and CH₄ concentrations from both the inversion system and aircraft. Posterior CO₂ concentration is in good agreement with the observed profile with biases of 1-5 ppm even in the upper troposphere,



320



whereas posterior CH₄ concentration profile shows systematic negative bias of 40–50 ppb from the boundary layer to the midtroposphere. We speculate that the persistence of these CH₄ bias is associated with the negative bias of the EGG4 data over the Korean Peninsula and discrepancies in oceanic emissions between the EGG4 and EDGAR datasets. Although EGG4 and EDGAR report comparable total annual inland CH₄ emission for the South Korea (1.81 and 1.87 Tg CH₄, respectively), its total emission within the total model domain is larger in EGG4 (6.83 Tg CH₄) than in EDGAR (4.51 Tg CH₄), largely due to a maritime baseline in EGG4 (~0.001 Tg grid⁻¹ yr⁻¹) whereas EDGAR is near zero over the ocean excluding shipping lanes. These differences likely contribute to the observed variations in ocean-grid concentrations. Our findings suggest that the underlying mechanisms for the maritime CH₄ source in EGG4 necessitate further investigation and additional observational constraints help to improve CH₄ budgets over the Korean Peninsula.

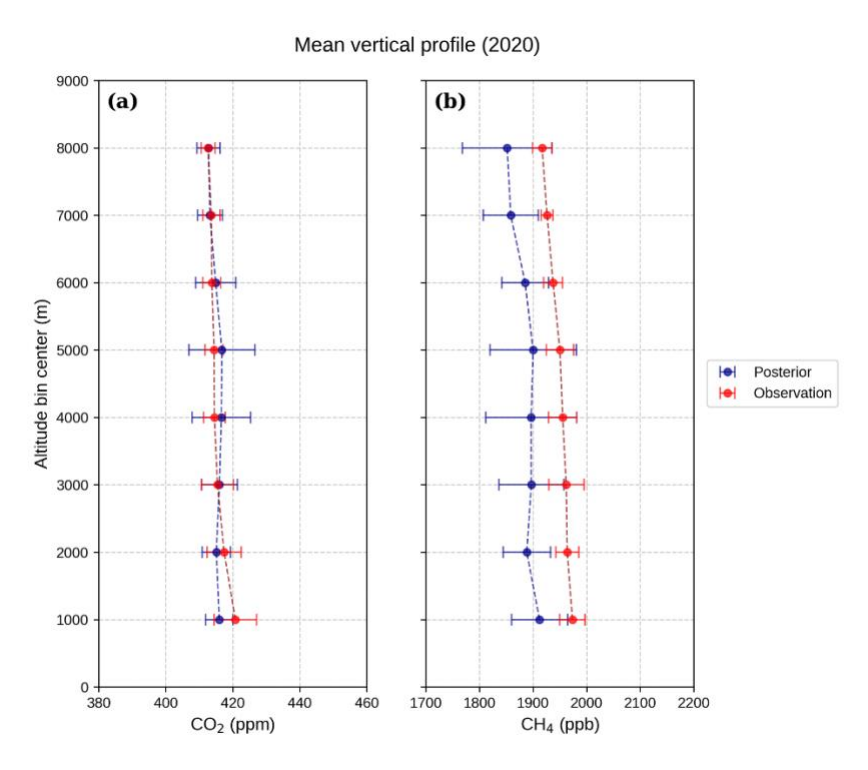


Figure 5. Mean vertical profiles of CO₂ and CH₄ from 10 CM-01 flights over South Korea in 2020. Profiles are aggregated into 1 km altitude bins (±500 m). Symbols and error bars show mean concentrations and associated uncertainties per bin: observations (red) and posterior (blue). Observation uncertainties combine measurement precision and sampling variability.

6.3 Uncertainty reduction in concentrations and fluxes

Figures 6 and 7 illustrate spatial distributions of ensemble spreads for CO₂ and CH₄ concentrations and the corresponding emission uncertainties respectively, showing prior uncertainties (left panels) and uncertainty reductions after the DA (right



340

345

350

355

360



panels). Unless noted, "reduction" denotes (posterior spread / prior spread – 1) × 100 % over grid cells. Domain-averaged flux uncertainty over land decreases by 25-35 % for CO₂ and about 20 % for CH₄, with local reductions up to 50 % near the observation sites. Prior uncertainties in both concentrations and anthropogenic fluxes are elevated over strong source regions in urban region (SMA), large-scale power plants along the MWI, and mid- and SCI and SEI for CO₂. Elevated uncertainties for CH₄ are observed in landfills around the SMA, and rice cultivation area and livestock farms (CLA) and coal-related emission region in northeastern China (NEC) (compare Fig. 2 with Fig. 6 and 7). Posterior uncertainties in GHG concentrations decrease substantially within an influence radius of about 90 km (e-folding distance) from all the stations. CH₄ certainty reduction reaches up to 40 % around the station and has a larger relative decrease than CO₂. This is consistent with negative bias in CH₄ concentration discussed above.

The spatial patterns of prior flux uncertainties closely resemble those for concentrations. Overall uncertainties for CO₂ emission decrease by about 7 % after the DA. CO₂ emission uncertainties decrease sharply within the influence radius of the AMY station along the western coasts, particularly for CO₂, where strong anthropogenic GHG sources are located (Fig. 7). Smaller reductions around ULD/GSN (< 5 %) reflect distance from major southeastern sources and prevailing winds. CH₄ emission uncertainties show the similar pattern with those of CO₂ except that the error reduction is relatively smaller than that of CO₂. Posterior flux uncertainty around the AMY produces a relatively smaller reduction in CH₄ compared to CO₂, primarily because major CH₄ sources are located more easterly than those of CO₂. These findings propose an observation network priority for additional CO₂ measurements in the southeastern industrial corridor and enhanced CH₄ coverage over central inland hotspots.

6.4 Posterior fluxes and concentrations of CO₂ and CH₄

Figures 8 and 9 show spatial distribution of CO₂ and CH₄ concentrations from EGG4 and from the inversion system, respectively. Both EGG4 and posterior GHG concentrations capture large-scale gradients and regional enhancements induced by both long-range transport and upwind source regions. Elevated CO₂ and CH₄ concentrations are apparent in heavy industry area and dense urbanized areas (boxed areas in Fig. 2). Over the Korean Peninsula, enhancements appear along the SMA, the west coast and southern industrial corridor (MWI, SCI, and SEI in Fig. 2) where power plants, traffic and industrial activities are major CO₂ emission sources and over central-western Korea (CLA in Fig. 2c) and northeastern region in China (NEC in Fig. 2c) where agriculture, landfills, and fossil fuel infrastructure are major CH₄ sources. Monthly EGG4 and posterior concentrations show persistent enhancements over the western Korean Peninsula and eastern China with winter accumulation and summer dilution (Fig. S8-S11). A comparison of the EGG4 concentration with the posterior concentrations shows notable spatial mismatch around the major hotspots of CO₂ and CH₄ emissions possibly because of wind bias and coarse resolution in EGG4. These results motivate a high-resolution regional inversion combining local priors, mesoscale meteorology, and continuous *in situ* observations, as implemented here. The SMA and MWI are major anthropogenic emission hotspots in the EDGAR and the top-down estimates, whereas EGG4 shows relatively smaller concentration of CO₂ and CH₄ in these regions



375

380

390

395



365 (Fig. 8a and 9a). Elevated CH₄ concentrations over the CLA appear more spatially diffuse in the EGG4 data. But the EGG4 data give wider and higher CO₂ and CH₄ concentrations in the north Korean Peninsula and NEC. Previous studies based on satellite products of the GOSAT and TROPOMI report the similar mismatch of CO₂ and CH₄ concentrations in coarse resolution global products in South Korea (Shim et al., 2019; Moon et al., 2024). Despite its representing regional gradients and seasonality of GHG concentrations, the 0.75° × 0.75° resolution of EGG4 is not enough to resolve the sharp urban-industrial emission heterogeneity and fine scale sources and sink of GHGs across Korea. They motivate the use of high-resolution regional inversion over complex terrain implemented here with the WRF-Chem/DART framework developed here, which combines local priors, mesoscale meteorology, and continuous in situ observations to constrain emissions with greater spatial fidelity.

The overall spatial distribution of posterior CO₂ and CH₄ emissions aligns with the prior estimates, retaining key hotspots in the Korean Peninsula and northeast China (See Fig. 2b and 2c) (Fig. 10a and 10c). Local increments of anthropogenic CO₂ and CH₄ emissions (defined as the difference between posterior and prior anthropogenic fluxes) are evident after the ensemble adjustment on emission to better align with atmospheric observations. Negative increments of CO₂ emissions are concentrated in densely populated and traffic-heavy regions (SMA and MWI) and positive increments for CO₂ emission are observed along the east coast and in the southeastern industrial corridor (i.e., SCI and SEI) (Fig. 10b). Notably, positive increments for CH₄ emission are widespread across inland emission regions of rice paddy, livestock facilities, landfills, and power industry, suggesting possible underestimation of prior CH₄ emission inventory (Fig. 10d).

Increment patterns demonstrate the WRF-Chem/DART diagnoses and corrects regional inconsistencies between bottom-up fluxes and atmospheric observations and depend on combined influences of observation density, inventory quality, and atmospheric transport. Accordingly, it is important to approach this issue with caution, as this adjustment may represent an artifact related to the persistent underestimation of CH₄ concentrations in the EGG4 product previously discussed. Because boundary data for CH₄ concentrations appears low-biased, data assimilation can compensate it by increasing posterior emissions, especially near surface stations within the localization radius when boundary fields are not adjusted directly. Further investigation is required for better understanding of the effect of expanding high-precision *in situ* and upper-air observation network, bias of boundary conditions, and inflation parameters.

Figure 11 presents a comprehensive summary of total anthropogenic CO₂ and CH₄ emissions in South Korea in 2020, comparing posterior estimates from our inversion system with several widely utilized bottom-up inventories. In the case of CO₂, the comparison encompass various open-source reference emission datasets from the Open-source Data Inventory for Anthropogenic CO₂ (ODIAC) (Oda et al., 2018), the Fossil Fuel Data Assimilation System (FFDAS) (Rayner et al., 2010), the Gridded Daily Fossil CO₂ Emissions Dataset (GRACED) (Dou et al., 2023), EDGAR, and the national total anthropogenic emissions (excluding the Land Use, Land Use Change and Forestry sector) as reported in the Biennial Transparent Report of the Republic of Korea (ROK-BTR, hereafter). Despite methodological discrepancies including proxy choice, point-source treatment, spatial disaggregation, native resolution, and sectoral attribution making significant portion of the inter-inventory variation, the posterior estimates agree with the ROK-BTR at the national scale within the bounds of uncertainty for both





species (Fig. 11). Importantly, it is observed that the posterior CH₄ emissions diverge from the bottom-up estimates in contrast to the posterior CH₄ emissions.

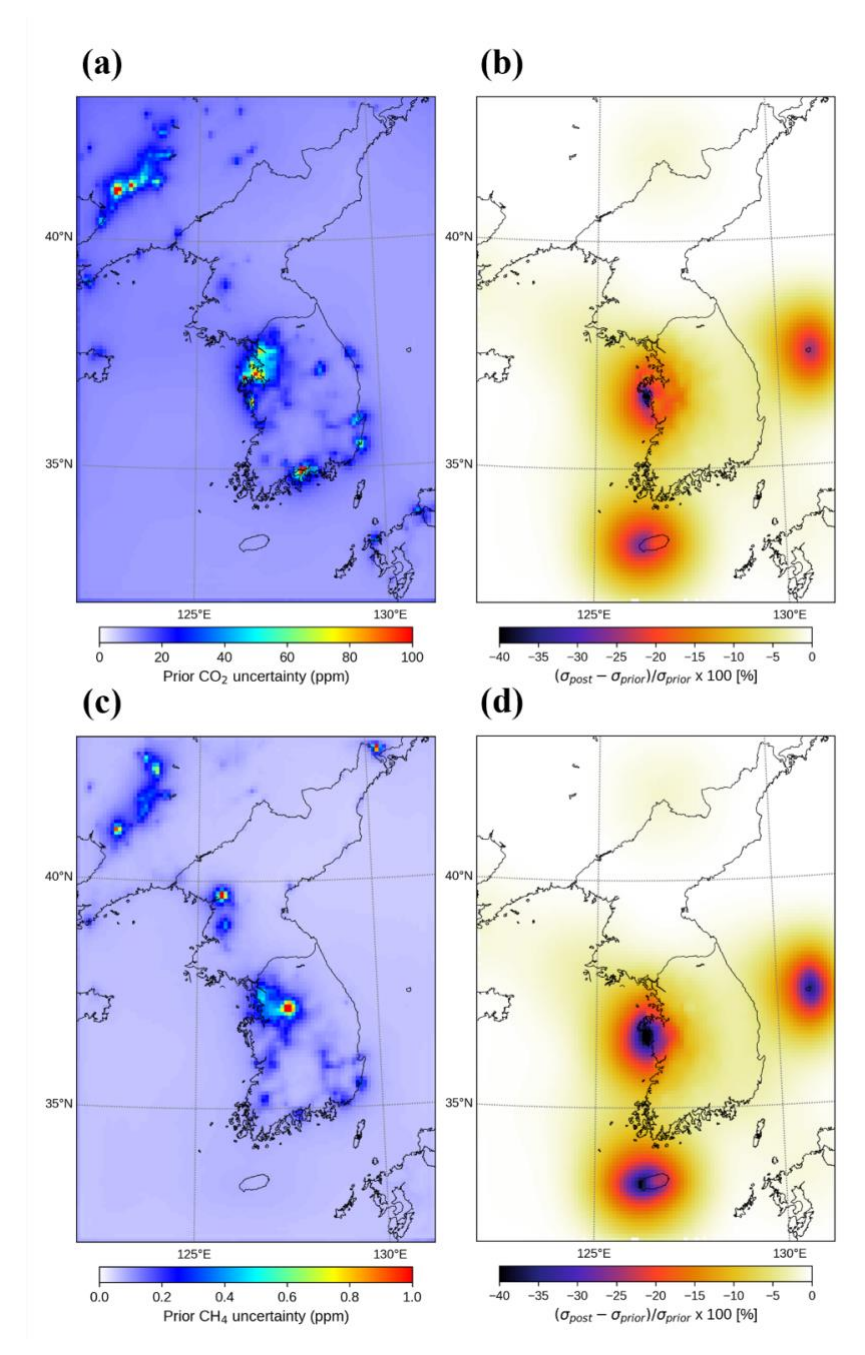


Figure 6. Annual prior concentration uncertainty (ensemble spread) (a,c) and its reduction after assimilation (b,d) for CO_2 (a,b) and CH_4 (c,d) in 2020.





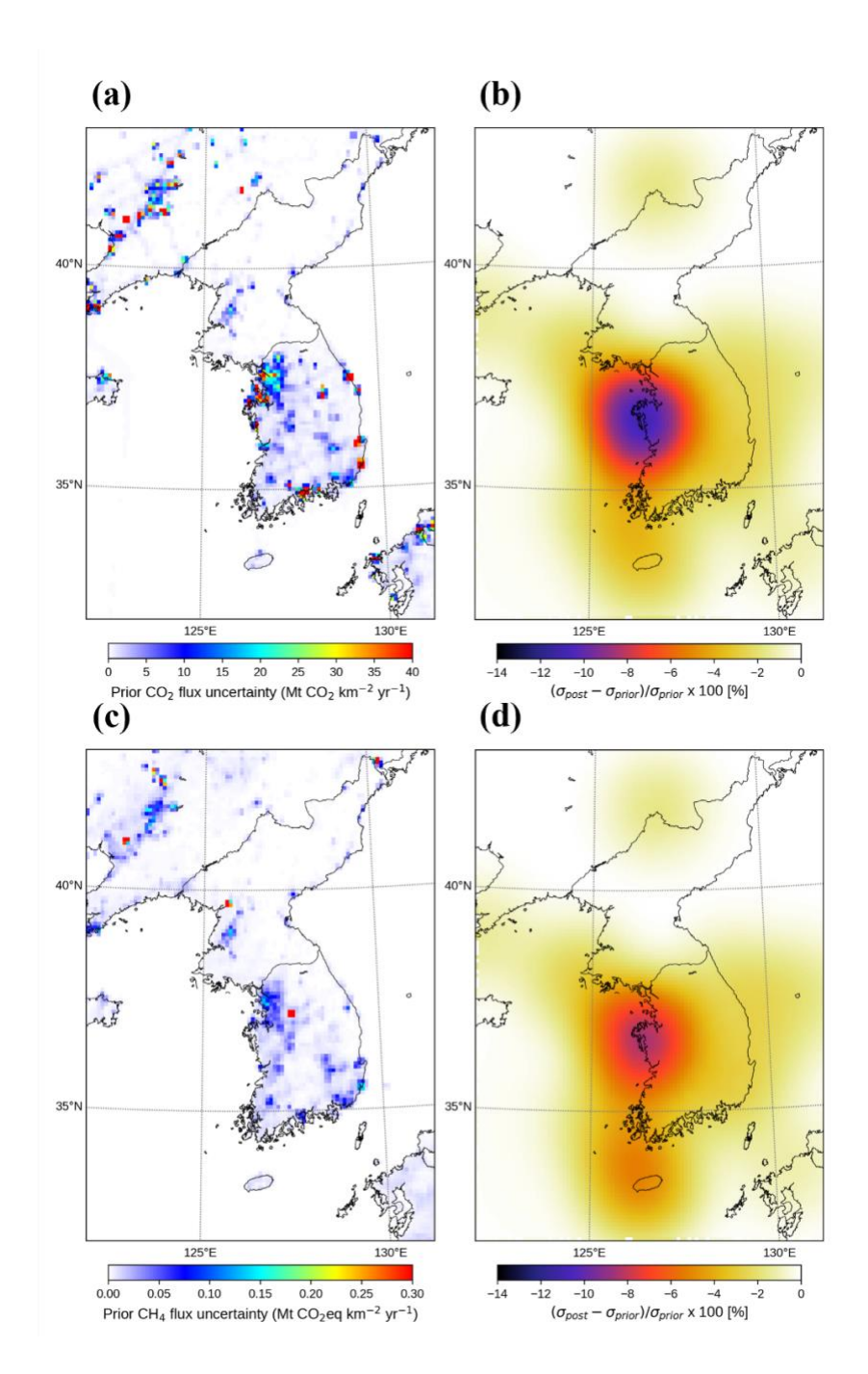
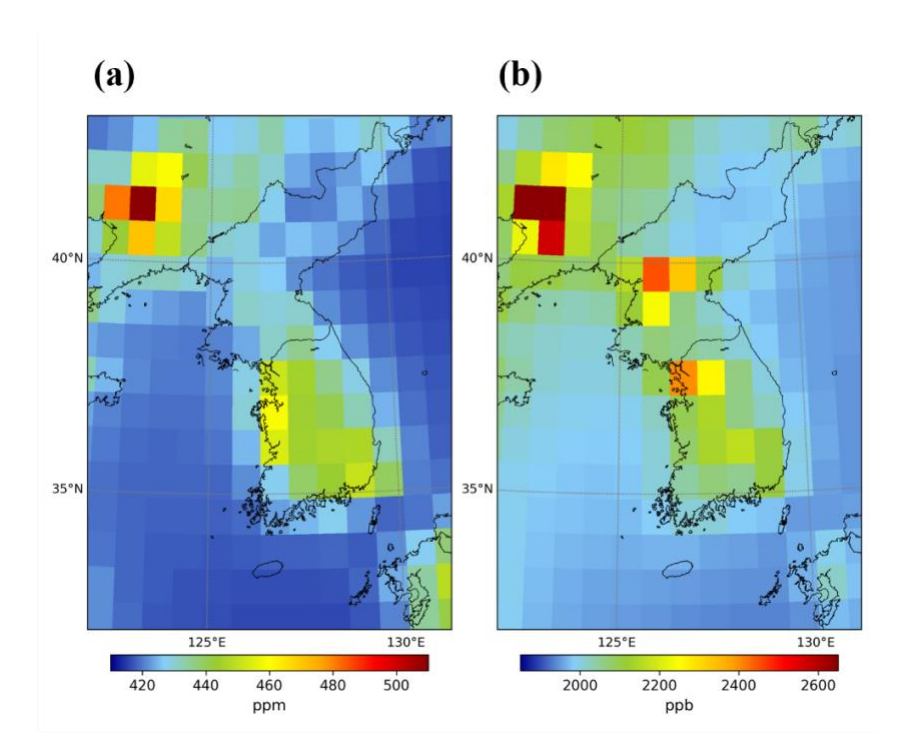


Figure 7. Annual prior flux uncertainty (a and c) and flux-uncertainty reduction (b and d) for CO₂ (a and b) and CH₄ (c and d) in 2020.







410 Figure 8. Annual mean surface concentrations of CO₂ (a) and CH₄ (b) over the Korean Peninsula in 2020 from the EGG4.

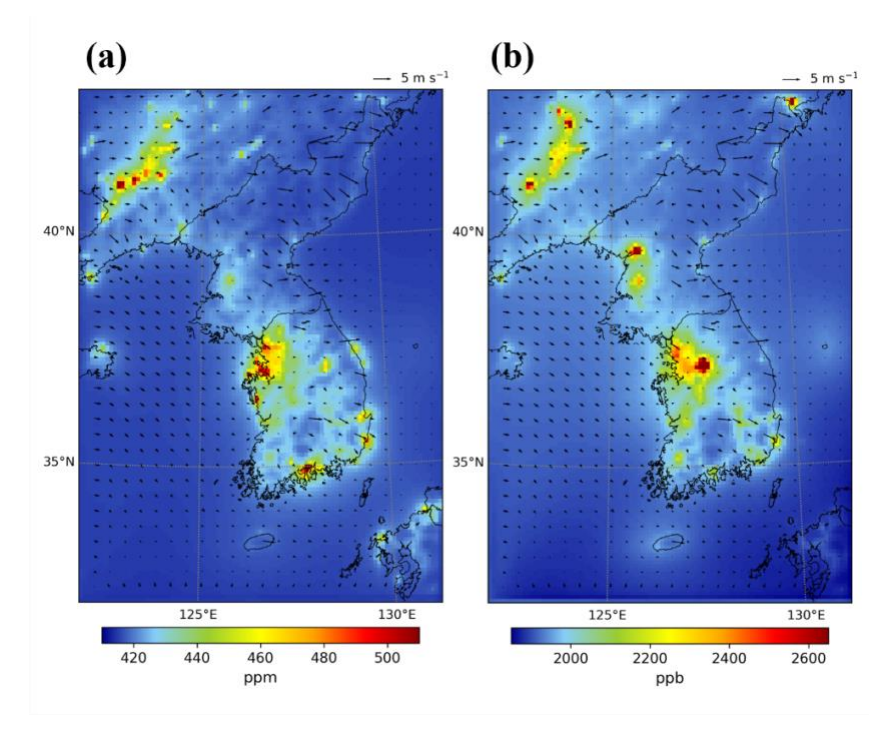


Figure 9. Annual mean surface posterior concentrations of CO₂ (a) and CH₄ (b) over the Korean Peninsula in 2020 from the WRF-Chem/DART inversion system. Wind vectors at 10m illustrate prevailing flow conditions that shape annual concentration gradients.





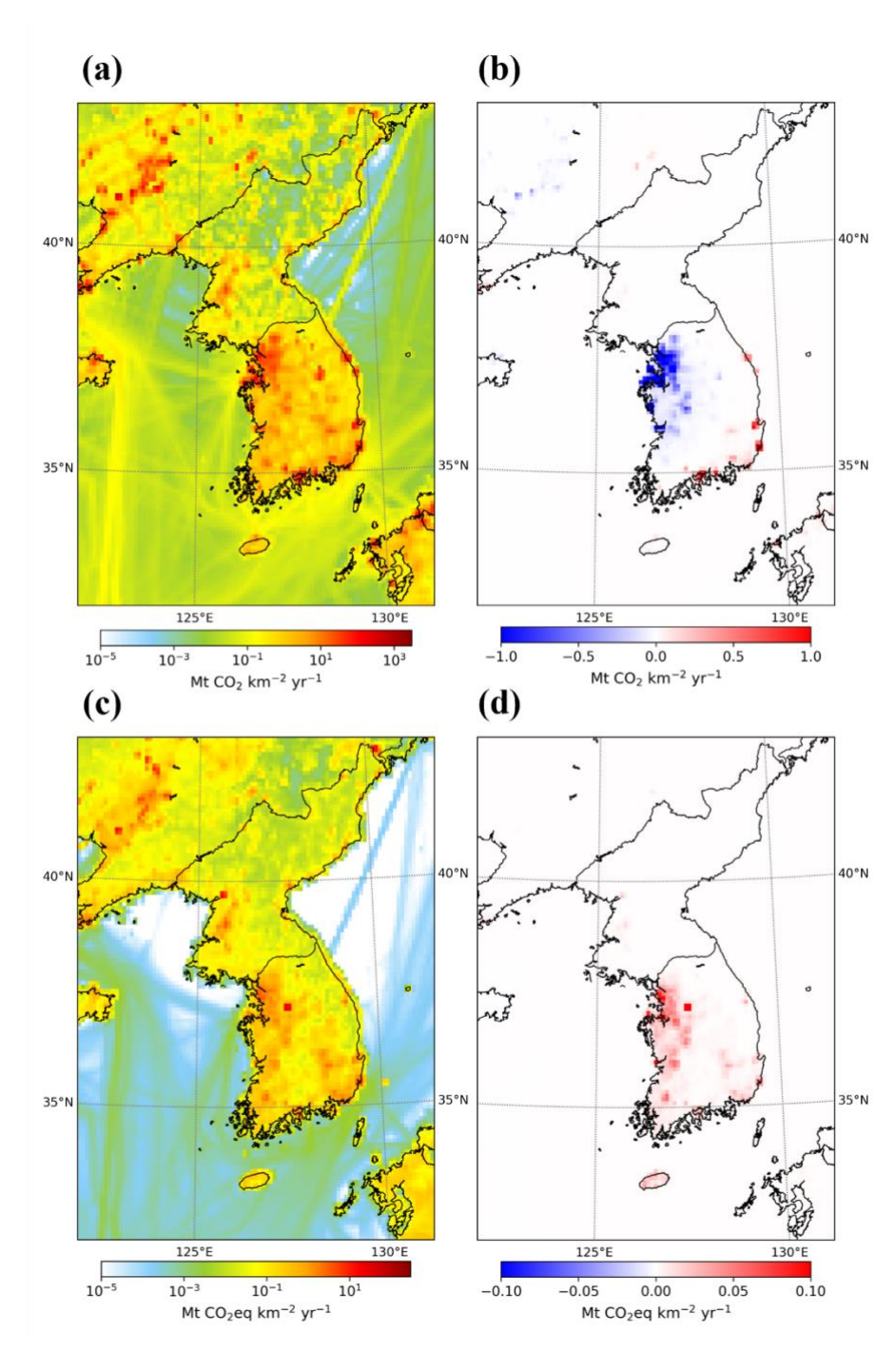


Figure 10. Annual-mean posterior surface fluxes (a and c) and assimilation increments (posterior minus prior) (b and d) for CO_2 (a and b) and CH_4 (c and d) from the WRF-Chem/DART system. Red (blue) shading indicates an increase (decrease) in the posterior relative to the prior.





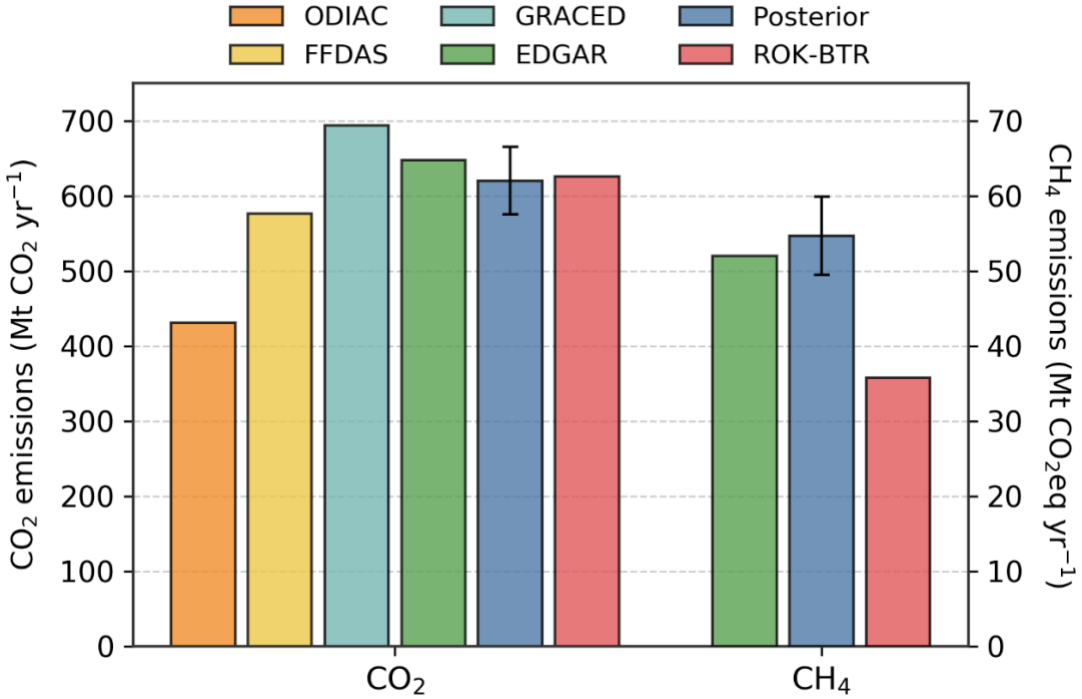


Figure 11. Annual total anthropogenic CO₂ and CH₄ emissions over South Korea in 2020 from multiple datasets. CO₂ comparisons include ODIAC, FFDAS, GRACED, EDGAR, ROK-BTR, and the posterior (six sources). CH₄ comparisons include EDGAR, ROK-BTR, and the posterior. Error bars denote posterior uncertainty. (FFDAS was scaled using the 2015–2020 gross emission growth rate from ROK-BTR because FFDAS is available only through 2015)

425 7 Summary and Conclusion

420

430

435

This study presents a high-resolution dual-species GHG (CO₂ and CH₄) inversion framework using the coupled WRF-Chem/DART system that assimilate continuous high-precision *in situ* observations of GHG concentrations. The system provides spatially explicit, observation-constrained emission estimates and dynamically consistent temporal state updates through ensemble data assimilation. This top-down estimate framework combines the model parameterizations for complex landscapes with the fully coupled treatment of meteorology and chemistry and facilitates dynamically consistent temporal state updates via ensemble data assimilation. The incorporation of precise high-frequency *in situ* observations further helps better representation of near-surface gradients, thereby enhancing anthropogenic flux sensitivity. The system complements the inventories by identifying spatial information and constraining its uncertainties.

Application to calendar year of 2020 produces reliable spatio-temporal variations of CO₂ and CH₄ emissions and reduces mismatch with the observed CO₂ and CH₄ concentrations at all high-precision observation sites. There are overall reductions in uncertainties and errors of the top-down estimates of GHG concentration and emission. The top-down system produces that mean bias error of surface CO₂ and CH₄ concentrations are much smaller than the EGG4 reanalysis data (1.2 ppm and 30 ppb)



440

445



at the high-precision surface observatory. We also find out that various CH₄ emission data should be checked especially over the ocean. Posterior national totals are consistent with the national inventory estimates of Korea (Republic of) within uncertainty, while revealing their regional discrepancies relative to the prior particularly in densely populated, industrial and agricultural areas. Posterior increments suggest that prior CO₂ emissions are likely overestimated over the Seoul Metropolitan Area and the western coastal region, while CH₄ emissions are underestimated in inland agricultural areas. These results provide an aggregate-level consistency check and underscore the value of top-down constraints for sub-national inventory refinement. Our high-resolution, dual-species WRF-Chem/DART inversion framework together with surface heterogeneity-aware parameterizations delivers spatially explicit emission estimates for policy assessments, operational monitoring, and verification within the national MMRV and international climate commitments across national, subnational, and city scales.

Code and Data availability

Model source code used in this study are archived on Zenodo under https://doi.org/10.5281/zenodo.16939122 (Kwon et al., 2025a). Preprocessed data, model output, and model configurations used in this study are archived on Zenodo under https://doi.org/10.5281/zenodo.16947463 (Kwon et al., 2025b). ERA5 is available after registration at 450 https://doi.org/10.24381/cds.adbb2d47 (pressure levels) (Hersbach et al., 2023a) and https://doi.org/10.24381/cds.bd0915c6 (single level) (Hersbach et al., 2023b). CAMS EGG4 is available after registration at https://doi.org/10.24381/cda4ed31 (Copernicus Atmosphere Monitoring Service, 2022). PREPBUFR is available at https://doi.org/10.5065/Z83F-N512 (National Centers for Environmental Prediction, 2008). EDGARv8.0 is available at https://edgar.jrc.ec.europa.eu/dataset_ghg80 (Crippa 455 et al., 2023). FFDAS is available at https://ffdas.rc.nau.edu/Data.html (Rayner et al., 2010). GRACED is available after registration https://carbonmonitor-graced.com (Dou 2023). **ODIAC** available et al., at https://doi.org/10.17595/20170411.001 (Oda et al., 2015). FINNv2.5 is available after registration at https://doi.org/10.5065/XNPA-AF09 (Wiedinmyer and Emmons, 2022). SeaFlux is available at https://doi.org/10.5281/zenodo.5482547 (Gregor and Fay, 2021). Annual budget of CO₂ and CH₄ emissions in South Korea is available under https://unfccc.int/documents/645637 (Biennial Transparency Report of Republic of Korea, 2025). 460 EDGARv8.0, FFDAS, GRACED and the Republic of Korea's Biennial Transparency Report are also archived on Zenodo under https://doi.org/10.5281/zenodo.17402804 (Kwon et al., 2025c).

465 Author contributions

DK, BK, ES, AA, CS, DS, SK, SJ, and JH conceptualized and designed the study. DK, BK, JL, JK, ES, and AA contributed to the implementation and development of the forward and inverse modeling framework. DS, SL, SK, and SJ were responsible





for the WMO/GAW KMA observation program and the aircraft-based measurement. DK and JA performed preprocessing and visualization of the VPRM inputs and outputs. DK and BK collected and processed the remaining input datasets, conducted the model simulations, and carried out the analysis and visualization. DK, BK, and JH prepared the original draft. All authors reviewed and edited the manuscript.

Competing interests

One of authors is a member of the editorial board of Geoscientific Model Development.

Acknowledgements

We sincerely thank the editor, staffs, and all the reviewers for their constructive comments and support, which significantly improved this paper. We received help from an AI tool for English improvement.

Financial support

This work was funded by the Korea Meteorological Administration Research and Development Program under Grant RS-2024-00404365.





References

505

- Agustí-Panareda, A., Barré, J., Massart, S., Inness, A., Aben, I., Ades, M., Baier, B. C., Balsamo, G., Borsdorff, T., Bousserez, N., Boussetta, S., Buchwitz, M., Cantarello, L., Crevoisier, C., Engelen, R., Eskes, H., Flemming, J., Garrigues, S.,
 Hasekamp, O., Huijnen, V., Jones, L., Kipling, Z., Langerock, B., McNorton, J., Meilhac, N., Noël, S., Parrington, M., Peuch, V.-H., Ramonet, M., Razinger, M., Reuter, M., Ribas, R., Suttie, M., Sweeney, C., Tarniewicz, J., and Wu, L.: Technical note: The CAMS greenhouse gas reanalysis from 2003 to 2020, Atmospheric Chemistry and Physics, 23, 3829–3859, https://doi.org/10.5194/acp-23-3829-2023, 2023.
- Ahmadov, R., Gerbig, C., Kretschmer, R., Koerner, S., Neininger, B., Dolman, A. J., and Sarrat, C.: Mesoscale covariance of transport and CO2 fluxes: Evidence from observations and simulations using the WRF-VPRM coupled atmosphere-biosphere model, Journal of Geophysical Research: Atmospheres, 112, https://doi.org/10.1029/2007JD008552, 2007.
 - Anderson, J., Hoar, T., Raeder, K., Liu, H., Collins, N., Torn, R., and Avellano, A.: The Data Assimilation Research Testbed:

 A Community Facility, Bulletin of the American Meteorological Society, 90, 1283–1296, https://doi.org/10.1175/2009BAMS2618.1, 2009.
- Anderson, J. L.: An Ensemble Adjustment Kalman Filter for Data Assimilation, Monthly Weather Review, 129, 2884–2903, https://doi.org/10.1175/1520-0493(2001)129<2884:AEAKFF>2.0.CO;2, 2001.
 - Anderson, J. L.: Localization and Sampling Error Correction in Ensemble Kalman Filter Data Assimilation, Monthly Weather Review, 140, 2359–2371, https://doi.org/10.1175/MWR-D-11-00013.1, 2012.
- Barker, D., Huang, X.-Y., Liu, Z., Auligné, T., Zhang, X., Rugg, S., Ajjaji, R., Bourgeois, A., Bray, J., Chen, Y., Demirtas,
 M., Guo, Y.-R., Henderson, T., Huang, W., Lin, H.-C., Michalakes, J., Rizvi, S., and Zhang, X.: The Weather Research and Forecasting Model's Community Variational/Ensemble Data Assimilation System: WRFDA, Bulletin of the American Meteorological Society, 93, 831–843, https://doi.org/10.1175/BAMS-D-11-00167.1, 2012.
 - Beck, V., Koch, T., Kretschmer, R., Marshall, J.and Ahmadov, R., Gerbig, C., Pillai, D., and Heimann, M.: The WRF Greenhouse Gas Model (WRF-GHG). Technical Report No. 25, Tech. rep., Max Planck Institute for Biogeochemistry, Jena, Germany, https://www.bgc-jena.mpg.de/5363366/tech report25.pdf, 2012.
 - Biennial Transparency Report of Republic of Korea [data set], https://unfccc.int/documents/645637 (last access: 22 October 2025), 2025.
 - Brunner, D., Suter, I., Bernet, L., Constantin, L., Grange, S. K., Rubli, P., Li, J., Chen, J., Bigi, A., and Emmenegger, L.: Building-resolving simulations of anthropogenic and biospheric CO₂ in the city of Zurich with GRAMM/GRAL, EGUsphere, 1–34, https://doi.org/10.5194/egusphere-2025-640, 2025.
 - Bukosa, B., Mikaloff-Fletcher, S., Brailsford, G., Smale, D., Keller, E. D., Baisden, W. T., Kirschbaum, M. U. F., Giltrap, D. L., Liáng, L., Moore, S., Moss, R., Nichol, S., Turnbull, J., Geddes, A., Kennett, D., Hidy, D., Barcza, Z., Schipper, L. A., Wall, A. M., Nakaoka, S.-I., Mukai, H., and Brandon, A.: Inverse modelling of New Zealand's carbon dioxide balance estimates a larger than expected carbon sink, EGUsphere, 1–41, https://doi.org/10.5194/egusphere-2024-3866, 2025.



2023.

530

535

540



- Bréon, F. M., Broquet, G., Puygrenier, V., Chevallier, F., Xueref-Remy, I., Ramonet, M., Dieudonné, E., Lopez, M., Schmidt, M., Perrussel, O., and Ciais, P.: An attempt at estimating Paris area CO₂ emissions from atmospheric concentration measurements, Atmospheric Chemistry and Physics, 15, 1707–1724, https://doi.org/10.5194/acp-15-1707-2015, 2015.
- Byrne, B., Baker, D. F., Basu, S., Bertolacci, M., Bowman, K. W., Carroll, D., Chatterjee, A., Chevallier, F., Ciais, P., Cressie, N., Crisp, D., Crowell, S., Deng, F., Deng, Z., Deutscher, N. M., Dubey, M. K., Feng, S., García, O. E., Griffith, D. W. T.,
 Herkommer, B., Hu, L., Jacobson, A. R., Janardanan, R., Jeong, S., Johnson, M. S., Jones, D. B. A., Kivi, R., Liu, J., Liu, Z., Maksyutov, S., Miller, J. B., Miller, S. M., Morino, I., Notholt, J., Oda, T., O'Dell, C. W., Oh, Y.-S., Ohyama, H., Patra, P. K., Peiro, H., Petri, C., Philip, S., Pollard, D. F., Poulter, B., Remaud, M., Schuh, A., Sha, M. K., Shiomi, K., Strong, K., Sweeney, C., Té, Y., Tian, H., Velazco, V. A., Vrekoussis, M., Warneke, T., Worden, J. R., Wunch, D., Yao, Y., Yun, J., Zammit-Mangion, A., and Zeng, N.: National CO₂ budgets (2015–2020) inferred from atmospheric CO₂ observations in support of the global stocktake, Earth System Science Data, 15, 963–1004, https://doi.org/10.5194/essd-15-963-2023,
 - Callewaert, S., Brioude, J., Langerock, B., Duflot, V., Fonteyn, D., Müller, J.-F., Metzger, J.-M., Hermans, C., Kumps, N., Ramonet, M., Lopez, M., Mahieu, E., and De Mazière, M.: Analysis of CO₂, CH₄, and CO surface and column concentrations observed at Réunion Island by assessing WRF-Chem simulations, Atmospheric Chemistry and Physics, 22, 7763–7792, https://doi.org/10.5194/acp-22-7763-2022, 2022.
 - Copernicus Atmosphere Monitoring Service: CAMS global greenhouse gas reanalysis (EGG4), CAMS Atmosphere Data Store (ADS) [data set], https://doi.org/10.24380/8fck-9w87 (last access: 22 October 2025), 2021.
 - Crippa, M., Guizzardi D., Pagani F., Banja M., Muntean M., Schaaf E., Becker, W., Monforti-Ferrario F., Quadrelli, R., Risquez Martin, A., Taghavi-Moharamli, P., Grassi, G., Rossi, S., Brandao De Melo, J., Oom, D., Branco, A., San-Miguel, J., Vignati, E.: EDGAR v8.0 Greenhouse Gas Emissions, European Commission, Joint Research Centre (JRC) [data set] https://doi.org/10.2905/b54d8149-2864-4fb9-96b9-5fd3a020c224 (last access: 22 October 2025), 2023
 - Crippa, M., Guizzardi, D., Pagani, F., Schiavina, M., Melchiorri, M., Pisoni, E., Graziosi, F., Muntean, M., Maes, J., Dijkstra, L., Van Damme, M., Clarisse, L., and Coheur, P.: Insights into the spatial distribution of global, national, and subnational greenhouse gas emissions in the Emissions Database for Global Atmospheric Research (EDGAR v8.0), Earth System Science Data, 16, 2811–2830, https://doi.org/10.5194/essd-16-2811-2024, 2024.
 - Custódio, D., Borrego, C., and Relvas, H.: Worldwide evaluation of CAMS-EGG4 CO₂ data re-analysis at the surface level, Toxics, 10, 331, https://doi.org/10.3390/toxics10060331, 2022.
 - Dekker, I. N., Houweling, S., Aben, I., Röckmann, T., Krol, M., Martínez-Alonso, S., Deeter, M. N., and Worden, H. M.: Quantification of CO emissions from the city of Madrid using MOPITT satellite retrievals and WRF simulations, Atmospheric Chemistry and Physics, 17, 14675–14694, https://doi.org/10.5194/acp-17-14675-2017, 2017.
 - Deng, Z., Ciais, P., Tzompa-Sosa, Z. A., Saunois, M., Qiu, C., Tan, C., Sun, T., Ke, P., Cui, Y., Tanaka, K., Lin, X., Thompson, R. L., Tian, H., Yao, Y., Huang, Y., Lauerwald, R., Jain, A. K., Xu, X., Bastos, A., Sitch, S., Palmer, P. I., Lauvaux, T.,



560



- d'Aspremont, A., Giron, C., Benoit, A., Poulter, B., Chang, J., Petrescu, A. M. R., Davis, S. J., Liu, Z., Grassi, G., Albergel, C., Tubiello, F. N., Perugini, L., Peters, W., and Chevallier, F.: Comparing national greenhouse gas budgets reported in UNFCCC inventories against atmospheric inversions, Earth System Science Data, 14, 1639–1675, https://doi.org/10.5194/essd-14-1639-2022, 2022.
 - Denison, S., Forster, P. M., and Smith, C. J.: Guidance on emissions metrics for nationally determined contributions under the Paris Agreement, Environ. Res. Lett., 14, 124002, https://doi.org/10.1088/1748-9326/ab4df4, 2019.
- Dou, X., Hong, J., Ciais, P., Chevallier, F., Yan, F., Yu, Y., Hu, Y., Huo, D., Sun, Y., Wang, Y., Davis, S. J., Crippa, M.,
 Janssens-Maenhout, G., Guizzardi, D., Solazzo, E., Lin, X., Song, X., Zhu, B., Cui, D., Ke, P., Wang, H., Zhou, W., Huang,
 X., Deng, Z., and Liu, Z.: Near-real-time global gridded daily CO₂ emissions 2021, Sci Data, 10, 69,
 https://doi.org/10.1038/s41597-023-01963-0, 2023.
 - East, J. D., Jacob, D. J., Balasus, N., Bloom, A. A., Bruhwiler, L., Chen, Z., Kaplan, J. O., Mickley, L. J., Mooring, T. A., Penn, E., Poulter, B., Sulprizio, M. P., Worden, J. R., Yantosca, R. M., and Zhang, Z.: Interpreting the Seasonality of Atmospheric Methane, Geophysical Research Letters, 51, e2024GL108494, https://doi.org/10.1029/2024GL108494, 2024.
 - Elguindi, N., Granier, C., Stavrakou, T., Darras, S., Bauwens, M., Cao, H., Chen, C., Denier Van Der Gon, H. A. C., Dubovik, O., Fu, T. M., Henze, D. K., Jiang, Z., Keita, S., Kuenen, J. J. P., Kurokawa, J., Liousse, C., Miyazaki, K., Müller, J.-F., Qu, Z., Solmon, F., and Zheng, B.: Intercomparison of Magnitudes and Trends in Anthropogenic Surface Emissions From Bottom-Up Inventories, Top-Down Estimates, and Emission Scenarios, Earth's Future, 8, e2020EF001520, https://doi.org/10.1029/2020EF001520, 2020.Enting, I. G.: Inverse Problems in Atmospheric Constituent Transport, Cambridge University Press, Cambridge, https://doi.org/10.1017/CBO9780511535741, 2002.
 - Fay, A. R., Gregor, L., Landschützer, P., McKinley, G. A., Gruber, N., Gehlen, M., Iida, Y., Laruelle, G. G., Rödenbeck, C., Roobaert, A., and Zeng, J.: SeaFlux: harmonization of air–sea CO₂ fluxes from surface pCO₂ data products using a standardized approach, Earth System Science Data, 13, 4693–4710, https://doi.org/10.5194/essd-13-4693-2021, 2021.
- Feng, S., Lauvaux, T., Davis, K. J., Keller, K., Zhou, Y., Williams, C., Schuh, A. E., Liu, J., and Baker, I.: Seasonal Characteristics of Model Uncertainties From Biogenic Fluxes, Transport, and Large-Scale Boundary Inflow in Atmospheric CO₂ Simulations Over North America, Journal of Geophysical Research: Atmospheres, 124, 14325–14346, https://doi.org/10.1029/2019JD031165, 2019.
- Friedlingstein, P., O'Sullivan, M., Jones, M. W., Andrew, R. M., Hauck, J., Landschützer, P., Le Quéré, C., Li, H., Luijkx, I.
 T., Olsen, A., Peters, G. P., Peters, W., Pongratz, J., Schwingshackl, C., Sitch, S., Canadell, J. G., Ciais, P., Jackson, R. B., Alin, S. R., Arneth, A., Arora, V., Bates, N. R., Becker, M., Bellouin, N., Berghoff, C. F., Bittig, H. C., Bopp, L., Cadule, P., Campbell, K., Chamberlain, M. A., Chandra, N., Chevallier, F., Chini, L. P., Colligan, T., Decayeux, J., Djeutchouang, L. M., Dou, X., Duran Rojas, C., Enyo, K., Evans, W., Fay, A. R., Feely, R. A., Ford, D. J., Foster, A., Gasser, T., Gehlen, M., Gkritzalis, T., Grassi, G., Gregor, L., Gruber, N., Gürses, Ö., Harris, I., Hefner, M., Heinke, J., Hurtt, G. C., Iida, Y.,
 Ilyina, T., Jacobson, A. R., Jain, A. K., Jarníková, T., Jersild, A., Jiang, F., Jin, Z., Kato, E., Keeling, R. F., Klein Goldewijk,





- K., Knauer, J., Korsbakken, J. I., Lan, X., Lauvset, S. K., Lefèvre, N., Liu, Z., Liu, J., Ma, L., Maksyutov, S., Marland, G., Mayot, N., McGuire, P. C., Metzl, N., Monacci, N. M., Morgan, E. J., Nakaoka, S.-I., Neill, C., Niwa, Y., Nützel, T., Olivier, L., Ono, T., Palmer, P. I., Pierrot, D., Qin, Z., Resplandy, L., Roobaert, A., Rosan, T. M., Rödenbeck, C., Schwinger, J., Smallman, T. L., Smith, S. M., Sospedra-Alfonso, R., Steinhoff, T., Sun, Q., Sutton, A. J., Séférian, R., Takao, S., Tatebe, H., Tian, H., Tilbrook, B., Torres, O., Tourigny, E., Tsujino, H., Tubiello, F., van der Werf, G., Wanninkhof, R., Wang, X., Yang, D., Yang, X., Yu, Z., Yuan, W., Yue, X., Zaehle, S., Zeng, N., and Zeng, J.: Global Carbon Budget 2024, Earth Syst. Sci. Data, 17, 965–1039, https://doi.org/10.5194/essd-17-965-2025, 2025.
- Gaspari, G. and Cohn, S. E.: Construction of correlation functions in two and three dimensions, Quarterly Journal of the Royal Meteorological Society, 125, 723–757, https://doi.org/10.1002/qj.49712555417, 1999.
- Gaudet, B. J., Davis, K. J., Pal, S., Jacobson, A. R., Schuh, A., Lauvaux, T., Feng, S., and Browell, E. V.: Regional-Scale, Sector-Specific Evaluation of Global CO₂ Inversion Models Using Aircraft Data From the ACT-America Project, Journal of Geophysical Research: Atmospheres, 126, e2020JD033623, https://doi.org/10.1029/2020JD033623, 2021.
 - Gregor, L. and Fay, A.: SeaFlux: harmonised sea-air CO2 fluxes from surface pCO₂ data products using a standardised approach (2021.04.03), [data set], https://doi.org/10.5281/zenodo.5482547 (last access: 22 October 2025), 2021.
- 595 Grell, G. A., Peckham, S. E., Schmitz, R., McKeen, S. A., Frost, G., Skamarock, W. C., and Eder, B.: Fully coupled "online" chemistry within the WRF model, Atmospheric Environment, 39, 6957–6975, https://doi.org/10.1016/j.atmosenv.2005.04.027, 2005.
- Gurney, K. R., Law, R. M., Denning, A. S., Rayner, P. J., Baker, D., Bousquet, P., Bruhwiler, L., Chen, Y.-H., Ciais, P., Fan, S., Fung, I. Y., Gloor, M., Heimann, M., Higuchi, K., John, J., Maki, T., Maksyutov, S., Masarie, K., Peylin, P., Prather,
 M., Pak, B. C., Randerson, J., Sarmiento, J., Taguchi, S., Takahashi, T., and Yuen, C.-W.: Towards robust regional estimates of CO₂ sources and sinks using atmospheric transport models, Nature, 415, 626–630, https://doi.org/10.1038/415626a, 2002.
 - Harman, I. N.: The Role of Roughness Sublayer Dynamics Within Surface Exchange Schemes, Boundary-Layer Meteorol, 142, 1–20, https://doi.org/10.1007/s10546-011-9651-z, 2012.
- Harman, I. N. and Finnigan, J. J.: A simple unified theory for flow in the canopy and roughness sublayer, Boundary-Layer Meteorol, 123, 339–363, https://doi.org/10.1007/s10546-006-9145-6, 2007.
 - Harman, I. N. and Finnigan, J. J.: Scalar Concentration Profiles in the Canopy and Roughness Sublayer, Boundary-Layer Meteorol, 129, 323–351, https://doi.org/10.1007/s10546-008-9328-4, 2008.
- Henne, S., Brunner, D., Oney, B., Leuenberger, M., Eugster, W., Bamberger, I., Meinhardt, F., Steinbacher, M., and Emmenegger, L.: Validation of the Swiss methane emission inventory by atmospheric observations and inverse modelling, Atmospheric Chemistry and Physics, 16, 3683–3710, https://doi.org/10.5194/acp-16-3683-2016, 2016.
 - Hersbach, H., Bell, B., Berrisford, P., Biavati, G., Horányi, A., Muñoz Sabater, J., Nicolas, J., Peubey, C., Radu, R., Rozum, I., Schepers, D., Simmons, A., Soci, C., Dee, D., and Thépaut, J.-N.: ERA5 hourly data on pressure levels from 1959 to





- present, Copernicus Climate Change Service (C3S) Climate Data Store (CDS) [data set], https://doi.org/10.24381/cds.bd0915c6 (last access: 22 October 2025), 2023a.
 - Hersbach, H., Bell, B., Berrisford, P., Biavati, G., Horányi, A., Muñoz Sabater, J., Nicolas, J., Peubey, C., Radu, R., Rozum, I., Schepers, D., Simmons, A., Soci, C., Dee, D., and Thépaut, J.-N.: ERA5 hourly data on single levels from 1959 to present, Copernicus Climate Change Service (C3S) Climate Data Store (CDS) [data set], https://doi.org/10.24381/cds.adbb2d47 (last access: 22 October 2025), 2023b.
- Hersbach, H., Bell, B., Berrisford, P., Hirahara, S., Horányi, A., Muñoz-Sabater, J., Nicolas, J., Peubey, C., Radu, R., Schepers, D., Simmons, A., Soci, C., Abdalla, S., Abellan, X., Balsamo, G., Bechtold, P., Biavati, G., Bidlot, J., Bonavita, M., De Chiara, G., Dahlgren, P., Dee, D., Diamantakis, M., Dragani, R., Flemming, J., Forbes, R., Fuentes, M., Geer, A., Haimberger, L., Healy, S., J. Hogan, R., Hólm, E., Janisková, M., Keeley, S., Laloyaux, P., Lopez, P., Lupu, C., Radnoti, G., de Rosnay, P., Rozum, I., Vamborg, F., Villaume, S., Thépaut, J.-N.: The ERA5 global reanalysis, Q. J. Roy. Meteor.
 Soc., 146, 1999-2049, https://doi.org/10.1002/qi.3803, 2020.
 - Hilton, T. W., Davis, K. J., Keller, K., and Urban, N. M.: Improving North American terrestrial CO₂ flux diagnosis using spatial structure in land surface model residuals, Biogeosciences, 10, 4607–4625, https://doi.org/10.5194/bg-10-4607-2013, 2013.
- Hong, J. and Kim, J.: Impact of the Asian monsoon climate on ecosystem carbon and water exchanges: a wavelet analysis and its ecosystem modeling implications, Global Change Biology, 17, 1900–1916, https://doi.org/10.1111/j.1365-2486.2010.02337.x, 2011.
 - Hong, J.-W., Hong, J., Chun, J., Lee, Y. H., Chang, L.-S., Lee, J.-B., Yi, K., Park, Y.-S., Byun, Y.-H., and Joo, S.: Comparative assessment of net CO₂ exchange across an urbanization gradient in Korea based on eddy covariance measurements, Carbon Balance and Management, 14, 13, https://doi.org/10.1186/s13021-019-0128-6, 2019.
- Hong, J.-W., Lee, S.-D., Lee, K., and Hong, J.: Seasonal variations in the surface energy and CO₂ flux over a high-rise, high-population, residential urban area in the East Asian monsoon region, International Journal of Climatology, 40, 4384–4407, https://doi.org/10.1002/joc.6463, 2020.
 - Inness, A., Ades, M., Agustí-Panareda, A., Barré, J., Benedictow, A., Blechschmidt, A.-M., Dominguez, J. J., Engelen, R., Eskes, H., Flemming, J., Huijnen, V., Jones, L., Kipling, Z., Massart, S., Parrington, M., Peuch, V.-H., Razinger, M., Remy, S., Schulz, M., and Suttie, M.: The CAMS reanalysis of atmospheric composition, Atmospheric Chemistry and Physics, 19, 3515–3556, https://doi.org/10.5194/acp-19-3515-2019, 2019.
 - IPCC: Climate Change 2021: The Physical Science Basis. Contribution of Working Group I to the Sixth Assessment Report of the Intergovernmental Panel on Climate Change, edited by: Masson-Delmotte, V., Zhai, P., Pirani, A., Connors, S. L., Péan, C., Berger, S., Caud, N., Chen, Y., Goldfarb, L., Gomis, M. I., Huang, M., Leitzell, K., Lonnoy, E., Matthews, J. B.
- R., Maycock, T. K., Waterfield, T., Yelekçi, O., Yu, R., and Zhou, B., Cambridge University Press, https://doi.org/10.1017/9781009157896, 2021.



655

660

665

675



- Janssens-Maenhout, G., Crippa, M., Guizzardi, D., Muntean, M., Schaaf, E., Dentener, F., Bergamaschi, P., Pagliari, V., Olivier, J. G. J., Peters, J. A. H. W., van Aardenne, J. A., Monni, S., Doering, U., Petrescu, A. M. R., Solazzo, E., and Oreggioni, G. D.: EDGAR v4.3.2 Global Atlas of the three major greenhouse gas emissions for the period 1970–2012, Earth System Science Data, 11, 959–1002, https://doi.org/10.5194/essd-11-959-2019, 2019.
- Janssens-Maenhout, G., Pinty, B., Dowell, M., Zunker, H., Andersson, E., Balsamo, G., Bézy, J.-L., Brunhes, T., Bösch, H., Bojkov, B., Brunner, D., Buchwitz, M., Crisp, D., Ciais, P., Counet, P., Dee, D., Denier Van Der Gon, H., Dolman, H., Drinkwater, M. R., Dubovik, O., Engelen, R., Fehr, T., Fernandez, V., Heimann, M., Holmlund, K., Houweling, S., Husband, R., Juvyns, O., Kentarchos, A., Landgraf, J., Lang, R., Löscher, A., Marshall, J., Meijer, Y., Nakajima, M., Palmer, P. I., Peylin, P., Rayner, P., Scholze, M., Sierk, B., Tamminen, J., and Veefkind, P.: Toward an Operational Anthropogenic CO₂ Emissions Monitoring and Verification Support Capacity, Bulletin of the American Meteorological Society, 101, E1439–E1451, https://doi.org/10.1175/BAMS-D-19-0017.1, 2020.
- Jiménez, P. A., Dudhia, J., González-Rouco, J. F., Navarro, J., Montávez, J. P., and García-Bustamante, E.: A Revised Scheme for the WRF Surface Layer Formulation, Monthly Weather Review, 140, 898–918, https://doi.org/10.1175/MWR-D-11-00056.1, 2012.
- Jung, M., Henkel, K., Herold, M., and Churkina, G.: Exploiting synergies of global land cover products for carbon cycle modeling, Remote Sensing of Environment, 101, 534–553, https://doi.org/10.1016/j.rse.2006.01.020, 2006.
- Kang, J.-S., Kalnay, E., Miyoshi, T., Liu, J., and Fung, I.: Estimation of surface carbon fluxes with an advanced data assimilation methodology, Journal of Geophysical Research: Atmospheres, 117, https://doi.org/10.1029/2012JD018259, 2012.
- Kim, J., Shin, H.-J., Lee, K., and Hong, J.: Enhancement of ANN-based wind power forecasting by modification of surface roughness parameterization over complex terrain, Journal of Environmental Management, 362, 121246, https://doi.org/10.1016/j.jenvman.2024.121246, 2024.
- Kwon, D., Hong, J., and Koo, B.: WRF-Chem/DART inversion system for CO₂ and CH₄ emissions in Korea, Zenodo [data set], https://doi.org/10.5281/zenodo.16939122 (last access: 15 October 2025), 2025a
 - Kwon, D., Hong, J., and Koo, B.: WRF-Chem/DART inversion dataset for CO₂ and CH₄ emissions in Korea, Zenodo [data set], https://doi.org/10.5281/zenodo.16947463 (last access: 15 October 2025), 2025b
 - Kwon, D., Hong, J., and Koo, B.: Data for: Regional CO2 and CH4 inversion system using WRF-Chem (v4.4)/DART (v9.8.0) and continuous high-precision observations over the Korean Peninsula, Zenodo [data set], https://doi.org/10.5281/zenodo.17402804 (last access: 24 October 2025), 2025c
 - Lauvaux, T., Miles, N. L., Deng, A., Richardson, S. J., Cambaliza, M. O., Davis, K. J., Gaudet, B., Gurney, K. R., Huang, J., O'Keefe, D., Song, Y., Karion, A., Oda, T., Patarasuk, R., Razlivanov, I., Sarmiento, D., Shepson, P., Sweeney, C., Turnbull, J., and Wu, K.: High-resolution atmospheric inversion of urban CO2 emissions during the dormant season of the Indianapolis Flux Experiment (INFLUX), Journal of Geophysical Research: Atmospheres, 121, 5213–5236, https://doi.org/10.1002/2015JD024473, 2016.





- Lauvaux, T., Gurney, K. R., Miles, N. L., Davis, K. J., Richardson, S. J., Deng, A., Nathan, B. J., Oda, T., Wang, J. A., Hutyra, L., and Turnbull, J.: Policy-Relevant Assessment of Urban CO2 Emissions, Environ. Sci. Technol., 54, 10237–10245, https://doi.org/10.1021/acs.est.0c00343, 2020.
- Lee, H., Han, S.-O., Ryoo, S.-B., Lee, J.-S., and Lee, G.-W.: The measurement of atmospheric CO2 at KMA GAW regional stations, its characteristics, and comparisons with other East Asian sites, Atmospheric Chemistry and Physics, 19, 2149–2163, https://doi.org/10.5194/acp-19-2149-2019, 2019.
 - Lee, H., Seo, W., Li, S., Lee, S., Kenea, S. T., and Joo, S.: Measurement report: Atmospheric CH₄ at regional stations of the Korea Meteorological Administration–Global Atmosphere Watch Programme: measurement, characteristics, and long-term changes of its drivers, Atmos. Chem. Phys., 23, 7141–7159, https://doi.org/10.5194/acp-23-7141-2023, 2023.
- Lee, J. and Hong, J.: Implementation of spaceborne lidar-retrieved canopy height in the WRF model, Journal of Geophysical Research: Atmospheres, 121, 6863–6876, https://doi.org/10.1002/2015JD024299, 2016.
 - Lee, J., Hong, J., Noh, Y., and Jiménez, P. A.: Implementation of a roughness sublayer parameterization in the Weather Research and Forecasting model (WRF version 3.7.1) and its evaluation for regional climate simulations, Geoscientific Model Development, 13, 521–536, https://doi.org/10.5194/gmd-13-521-2020, 2020.
- Lee, K., Hong, J.-W., Kim, J., and Hong, J.: Partitioning of net CO₂ exchanges at the city-atmosphere interface into biotic and abiotic components, MethodsX, 8, 101231, https://doi.org/10.1016/j.mex.2021.101231, 2021.
 - Li, X., Hu, X.-M., Cai, C., Jia, Q., Zhang, Y., Liu, J., Xue, M., Xu, J., Wen, R., and Crowell, S. M. R.: Terrestrial CO₂ Fluxes, Concentrations, Sources and Budget in Northeast China: Observational and Modeling Studies, Journal of Geophysical Research: Atmospheres, 125, e2019JD031686, https://doi.org/10.1029/2019JD031686, 2020.
- 700 Liu, X., Mizzi, A. P., Anderson, J. L., Fung, I., and Cohen, R. C.: Assimilation of satellite NO2 observations at high spatial resolution using OSSEs, Atmospheric Chemistry and Physics, 2017.
 - Locatelli, R., Bousquet, P., Chevallier, F., Fortems-Cheney, A., Szopa, S., Saunois, M., Agusti-Panareda, A., Bergmann, D., Bian, H., Cameron-Smith, P., Chipperfield, M. P., Gloor, E., Houweling, S., Kawa, S. R., Krol, M., Patra, P. K., Prinn, R. G., Rigby, M., Saito, R., and Wilson, C.: Impact of transport model errors on the global and regional methane emissions estimated by inverse modelling, Atmospheric Chemistry and Physics, 13, 9917–9937, https://doi.org/10.5194/acp-13-9917-2013, 2013.
 - Ma, C., Wang, T., Jiang, Z., Wu, H., Zhao, M., Zhuang, B., Li, S., Xie, M., Li, M., Liu, J., and Wu, R.: Importance of Bias Correction in Data Assimilation of Multiple Observations Over Eastern China Using WRF-Chem/DART, Journal of Geophysical Research: Atmospheres, 125, e2019JD031465, https://doi.org/10.1029/2019JD031465, 2020.
- Mahadevan, P., Wofsy, S. C., Matross, D. M., Xiao, X., Dunn, A. L., Lin, J. C., Gerbig, C., Munger, J. W., Chow, V. Y., and Gottlieb, E. W.: A satellite-based biosphere parameterization for net ecosystem CO₂ exchange: Vegetation Photosynthesis and Respiration Model (VPRM), Global Biogeochemical Cycles, 22, https://doi.org/10.1029/2006GB002735, 2008.





- Ministry of Environment, Republic of Korea: The Republic of Korea's First Biennial Transparency Report and Fifth National Communication under the UNFCCC and the Paris Agreement, available at: https://unfccc.int/documents/645637 (last access: 06 June 2025), 2025.
- Mizzi, A. P., Arellano Jr., A. F., Edwards, D. P., Anderson, J. L., and Pfister, G. G.: Assimilating compact phase space retrievals of atmospheric composition with WRF-Chem/DART: a regional chemical transport/ensemble Kalman filter data assimilation system, Geophysical Model Development, 2016.
- Mizzi, A. P., Edwards, D. P., and Anderson, J. L.: Assimilating compact phase space retrievals (CPSRs): comparison with independent observations (MOZAIC in situ and IASI retrievals) and extension to assimilation of truncated retrieval profiles, Geoscientific Model Development, 11, 3727–3745, https://doi.org/10.5194/gmd-11-3727-2018, 2018.
 - Moon, J., Shim, C., Seo, J., and Han, J.: Evaluation of Korean methane emission sources with satellite retrievals by spatial correlation analysis, Environ Monit Assess, 196, 296, https://doi.org/10.1007/s10661-024-12449-w, 2024.
- Mueller, K. L., Lauvaux, T., Gurney, K. R., Roest, G., Ghosh, S., Gourdji, S. M., Karion, A., DeCola, P., and Whetstone, J.:

 An emerging GHG estimation approach can help cities achieve their climate and sustainability goals, Environ. Res. Lett.,

 16, 084003, https://doi.org/10.1088/1748-9326/ac0f25, 2021.
 - Nalini, K., Lauvaux, T., Abdallah, C., Lian, J., Ciais, P., Utard, H., Laurent, O., and Ramonet, M.: High-Resolution Lagrangian Inverse Modeling of CO₂ Emissions Over the Paris Region During the First 2020 Lockdown Period, Journal of Geophysical Research: Atmospheres, 127, e2021JD036032, https://doi.org/10.1029/2021JD036032, 2022.
- National Centers for Environmental Prediction, National Weather Service, NOAA, and U.S. Department of Commerce: NCEP ADP Global Upper Air and Surface Weather Observations (PREPBUFR format), Research Data Archive at the National Center for Atmospheric Research, Computational and Information Systems Laboratory [data set], https://doi.org/10.5065/Z83F-N512 (last access: 22 October 2025), 2008.
- Nisbet, E. G., Manning, M. R., Dlugokencky, E. J., Fisher, R. E., Lowry, D., Michel, S. E., Myhre, C. L., Platt, S. M., Allen,
 G., Bousquet, P., Brownlow, R., Cain, M., France, J. L., Hermansen, O., Hossaini, R., Jones, A. E., Levin, I., Manning, A. C., Myhre, G., Pyle, J. A., Vaughn, B. H., Warwick, N. J., and White, J. W. C.: Very Strong Atmospheric Methane Growth in the 4 Years 2014–2017: Implications for the Paris Agreement, Global Biogeochemical Cycles, 33, 318–342, https://doi.org/10.1029/2018GB006009, 2019.
- Oda, T. and Maksyutov, S.: ODIAC Fossil Fuel CO₂ Emissions Dataset (Version name: ODIAC2022), Center for Global Environmental Research, National Institute for Environmental Studies [data set], https://doi.org/10.17595/20170411.001 (last access: 22 October 2025), 2015.
 - Oda, T., Maksyutov, S., and Andres, R. J.: The Open-source Data Inventory for Anthropogenic CO₂, version 2016 (ODIAC2016): a global monthly fossil fuel CO₂ gridded emissions data product for tracer transport simulations and surface flux inversions, Earth System Science Data, 10, 87–107, https://doi.org/10.5194/essd-10-87-2018, 2018.



750



- Oda, T., Bun, R., Kinakh, V., Topylko, P., Halushchak, M., Marland, G., Lauvaux, T., Jonas, M., Maksyutov, S., Nahorski, Z., Lesiv, M., Danylo, O., and Horabik-Pyzel, J.: Errors and uncertainties in a gridded carbon dioxide emissions inventory, Mitig Adapt Strateg Glob Change, 24, 1007–1050, https://doi.org/10.1007/s11027-019-09877-2, 2019.
 - Ogle, S. M., Buendia, L., Butterbach-Bahl, K., Breidt, F. J., Hartman, M., Yagi, K., Nayamuth, R., Spencer, S., Wirth, T., and Smith, P.: Advancing national greenhouse gas inventories for agriculture in developing countries: improving activity data, emission factors and software technology, Environ. Res. Lett., 8, 015030, https://doi.org/10.1088/1748-9326/8/1/015030, 2013.
 - Pauw, W. P., Klein, R. J. T., Mbeva, K., Dzebo, A., Cassanmagnago, D., and Rudloff, A.: Beyond headline mitigation numbers: we need more transparent and comparable NDCs to achieve the Paris Agreement on climate change, Climatic Change, 147, 23–29, https://doi.org/10.1007/s10584-017-2122-x, 2018.
- Pisso, I., Patra, P., Takigawa, M., Machida, T., Matsueda, H., and Sawa, Y.: Assessing Lagrangian inverse modelling of urban anthropogenic CO₂ fluxes using in situ aircraft and ground-based measurements in the Tokyo area, Carbon Balance and Management, 14, 6, https://doi.org/10.1186/s13021-019-0118-8, 2019.
 - Rayner, P. J., Raupach, M. R., Paget, M., Peylin, P., and Koffi, E.: A new global gridded data set of CO₂ emissions from fossil fuel combustion: Methodology and evaluation, Journal of Geophysical Research: Atmospheres, 115, https://doi.org/10.1029/2009JD013439, 2010.
 - Rogelj, J., Den Elzen, M., Höhne, N., Fransen, T., Fekete, H., Winkler, H., Schaeffer, R., Sha, F., Riahi, K., and Meinshausen, M.: Paris Agreement climate proposals need a boost to keep warming well below 2 °C, Nature, 534, 631–639, https://doi.org/10.1038/nature18307, 2016.
- Roobaert, A., Laruelle, G. G., Landschützer, P., and Regnier, P.: Uncertainty in the global oceanic CO₂ uptake induced by wind forcing: quantification and spatial analysis, Biogeosciences, 15, 1701–1720, https://doi.org/10.5194/bg-15-1701-2018, 2018.
 - Roobaert, A., Laruelle, G. G., Landschützer, P., Gruber, N., Chou, L., and Regnier, P.: The Spatiotemporal Dynamics of the Sources and Sinks of CO₂ in the Global Coastal Ocean, Global Biogeochemical Cycles, 33, 1693–1714, https://doi.org/10.1029/2019GB006239, 2019.
- Schroeder, W., Oliva, P., Giglio, L., and Csiszar, I. A.: The New VIIRS 375 m active fire detection data product: Algorithm description and initial assessment, Remote Sensing of Environment, 143, 85–96, https://doi.org/10.1016/j.rse.2013.12.008, 2014.
 - Segato, D., Graziosi, F., and Manca, G.: Evaluation of Copernicus atmosphere monitoring service methane products 2019-2023, Publications Office of the European Union, https://data.europa.eu/doi/10.2760/8653047, 2025.
- Shim, C., Han, J., Henze, D. K., and Yoon, T.: Identifying local anthropogenic CO₂ emissions with satellite retrievals: a case study in South Korea, International Journal of Remote Sensing, 40, 1011–1029, https://doi.org/10.1080/01431161.2018.1523585, 2019.



780



- Sijikumar, S., Raju, A., Valsala, V., Tiwari, Y., Girach, I. A., Jain, C. D., and Ratnam, M. V.: High-Resolution Bayesian Inversion of Carbon Dioxide Flux Over Peninsular India, Atmospheric Environment, 308, 119868, https://doi.org/10.1016/j.atmosenv.2023.119868, 2023.
- Super, I., Denier van der Gon, H. A. C., van der Molen, M. K., Sterk, H. A. M., Hensen, A., and Peters, W.: A multi-model approach to monitor emissions of CO₂ and CO from an urban–industrial complex, Atmospheric Chemistry and Physics, 17, 13297–13316, https://doi.org/10.5194/acp-17-13297-2017, 2017.
- UNFCCC: Adoption of the Paris Agreement. Report No. FCCC/CP/2015/L.9/ Rev.1, available at: https://unfccc.int/resource/docs/2015/cop21/eng/109r01.pdf (last access: 22 October 2025), 2015.
 - van der Velde, I. R., Miller, J. B., van der Molen, M. K., Tans, P. P., Vaughn, B. H., White, J. W. C., Schaefer, K., and Peters, W.: The CarbonTracker Data Assimilation System for CO₂ and δ¹³C (CTDAS-C13 v1.0): retrieving information on land–atmosphere exchange processes, Geoscientific Model Development, 11, 283–304, https://doi.org/10.5194/gmd-11-283-2018, 2018.
- 790 Velasco, E., Segovia, E., and Roth, M.: High-resolution maps of carbon dioxide and moisture fluxes over an urban neighborhood, Environ. Sci.: Atmos., 3, 1110–1123, https://doi.org/10.1039/D2EA00108J, 2023.
 - Wang, Y., Yuan, Q., Li, T., Yang, Y., Zhou, S., and Zhang, L.: Seamless mapping of long-term (2010-2020) daily global XCO₂ and XCH₄ from the Greenhouse Gases Observing Satellite (GOSAT), Orbiting Carbon Observatory 2 (OCO-2), and CAMS global greenhouse gas reanalysis (CAMS-EGG4) with a spatiotemporally self-supervised fusion method, Earth System Science Data, 15, 3597-3622, https://doi.org/10.5194/essd-15-3597-2023, 2023.
 - Weiss, R. F. and Prinn, R. G.: Quantifying greenhouse-gas emissions from atmospheric measurements: a critical reality check for climate legislation, Philosophical Transactions of the Royal Society A: Mathematical, Physical and Engineering Sciences, 369, 1925–1942, https://doi.org/10.1098/rsta.2011.0006, 2011.
- Wiedinmyer, C. and Emmons, L.: Fire Inventory from NCAR version 2 Fire Emission. Research Data Archive at the National Roo Center for Atmospheric Research, Computational and Information Systems Laboratory [data set], https://doi.org/10.5065/XNPA-AF09 (last access: 22 October 2025), 2022.
 - Wiedinmyer, C., Akagi, S. K., Yokelson, R. J., Emmons, L. K., Al-Saadi, J. A., Orlando, J. J., and Soja, A. J.: The Fire INventory from NCAR (FINN): a high resolution global model to estimate the emissions from open burning, Geoscientific Model Development, 4, 625–641, https://doi.org/10.5194/gmd-4-625-2011, 2011.
- Wiedinmyer, C., Kimura, Y., McDonald-Buller, E. C., Emmons, L. K., Buchholz, R. R., Tang, W., Seto, K., Joseph, M. B., Barsanti, K. C., Carlton, A. G., and Yokelson, R.: The Fire Inventory from NCAR version 2.5: an updated global fire emissions model for climate and chemistry applications, Geoscientific Model Development, 16, 3873–3891, https://doi.org/10.5194/gmd-16-3873-2023, 2023.
- WMO: IG3IS Urban Greenhouse Gas Emission Observation and Monitoring Good Research Practice Guidelines, WMO GAW Report No 275, available at: https://library.wmo.int/idurl/4/58055, 2022.





- WMO: IG3IS National Scale Greenhouse Gas Emission Observation and Monitoring Good Practice Guidance, WMO GAW Report, in press, 2025.
- Zhang, Q., Li, M., Wang, M., Mizzi, A. P., Huang, Y., Wei, C., Jin, J., and Gu, Q.: CO₂ Flux over the Contiguous United States in 2016 Inverted by WRF-Chem/DART from OCO-2 XCO2 Retrievals, Remote Sensing, 13, 2996, https://doi.org/10.3390/rs13152996, 2021.
- Zhang, Q., Li, M., Wei, C., Mizzi, A. P., Huang, Y., and Gu, Q.: Assimilation of OCO-2 retrievals with WRF-Chem/DART:

 A case study for the Midwestern United States, Atmospheric Environment, 246, 118106, https://doi.org/10.1016/j.atmosenv.2020.118106, 2021.
- Zhao, X., Chen, J., Marshall, J., Gałkowski, M., Hachinger, S., Dietrich, F., Shekhar, A., Gensheimer, J., Wenzel, A., and Gerbig, C.: Understanding greenhouse gas (GHG) column concentrations in Munich using the Weather Research and Forecasting (WRF) model, Atmospheric Chemistry and Physics, 23, 14325–14347, https://doi.org/10.5194/acp-23-14325-2023, 2023.